Supplementary Materials for

Transformation of CO_2 to C_{2+} alcohols by tailoring the oxygen bonding via Fe-based tandem catalyst

Wenhang Wang[1,2,3]†, Xiangyu Guo[4,5]†, Yang Wang[1]*, Simin Lin[1], Xinhua Gao[6], Jie Liang[6], Jinqiang Zhang[7], Jinghao Xie[1], Hu Jiang[1], Fengliang Cao[1], Yongjie Chen[1], Guohui Yang[2], Thomas Frauenheim[5,8], Mingqing Wang[9], Tao Xing[9], Yiwu Lu[9], Qiang Liu[9], Kostya S. Novoselov[4,10]*, Noritatsu Tsubaki[2]*, Mingbo Wu[1]*

Corresponding author:
wangyang@upc.edu.cn (Y.W.);
kostya@nus.edu.sg (K.S.N.);
tsubaki@eng.u-toyama.ac.jp (N.T.);
wumb@upc.edu.cn (M.W.)

† These authors contributed equally to this work

The PDF file includes:

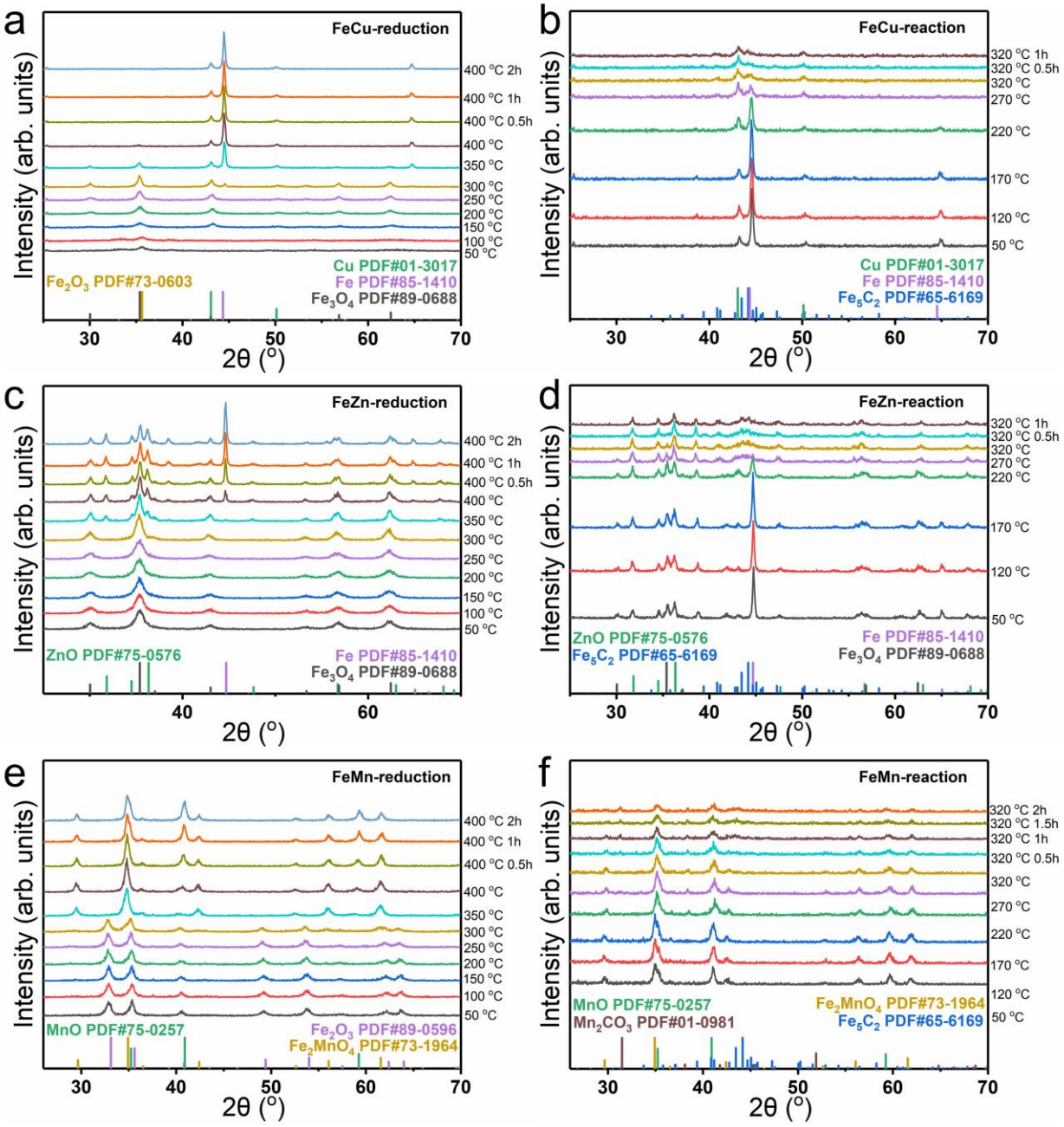

Supplementary Fig. 1. The structure analysis of FeX catalysts during reduction and reaction process. The in-situ XRD patterns of (a) FeCu reduction, (b) FeCu reaction, (c) FeZn reduction, (d) FeZn reaction, (e) FeMn reduction, and (f) FeMn reaction. Reduction conditions: H_2 flow rate of 60 ml min^{-1}. Reaction conditions: 0.8 MPa, $H_2/CO = 2$, 80 ml min^{-1}.

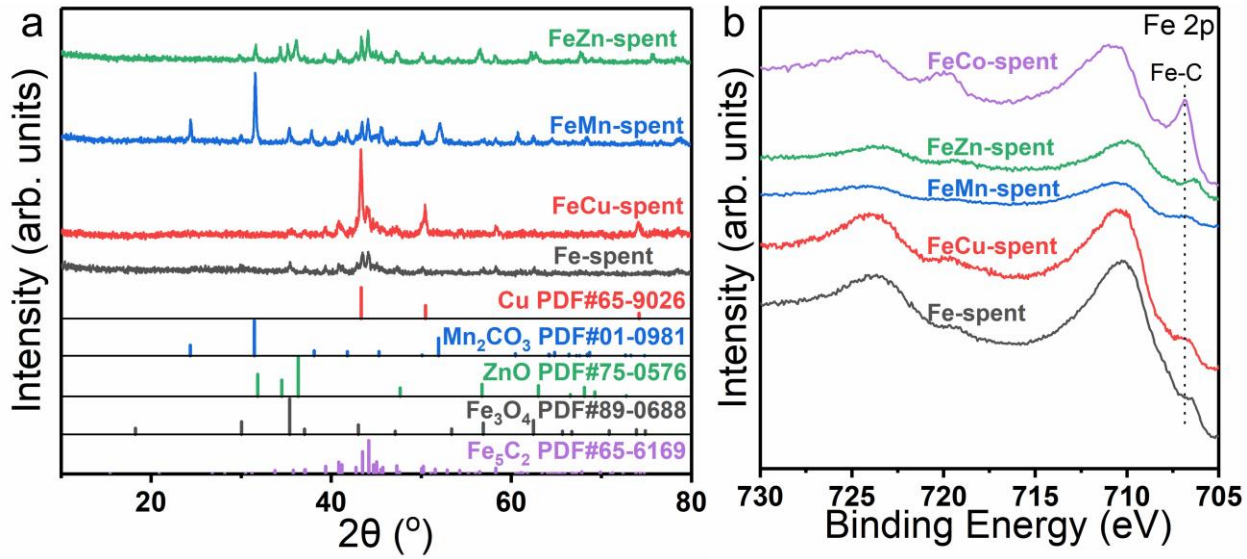

Supplementary Fig. 2. The structure analysis of spent FeX catalysts. (a) XRD patterns and (b) XPS spectra of series spent catalysts.

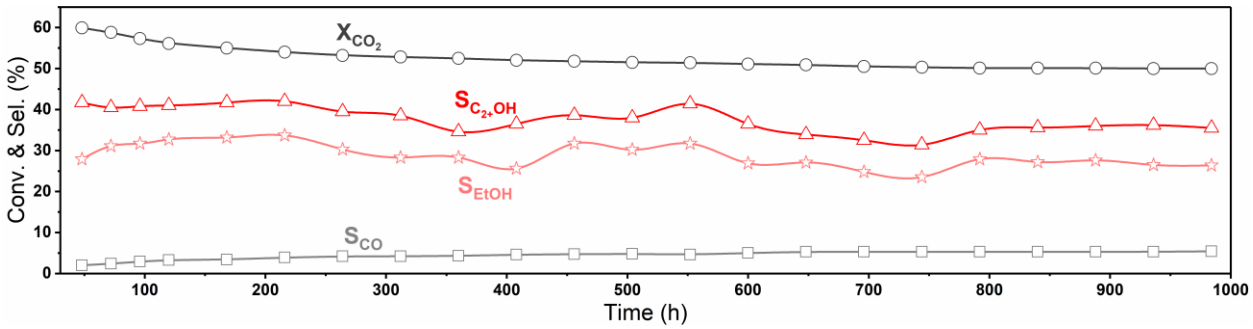

Supplementary Fig. 3. Long-term stability of FeCo&CZA catalyst. Reaction conditions: 320°C, 5.0 MPa, H_2/CO_2 = 3, 0.5 g, gas hourly space velocity at 1800 ml g_{cat}^{-1} h^{-1}.

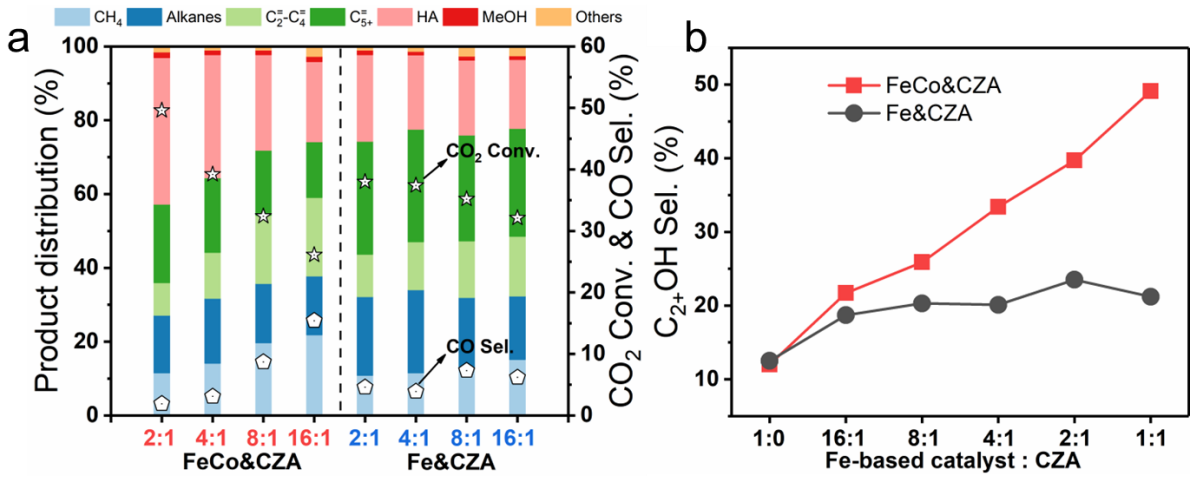

Supplementary Fig. 4. The reaction performance of the multifunctional catalysts with different CZA weights. Reaction conditions: 320 ℃, 5.0 MPa, H_2/CO_2 = 3:1, Fe-based catalyst of 0.1g and the weight of CZA is 1/*x* of Fe-based catalyst, TOS = 8h, 4500 ml g_{cat}^{-1} h^{-1}.

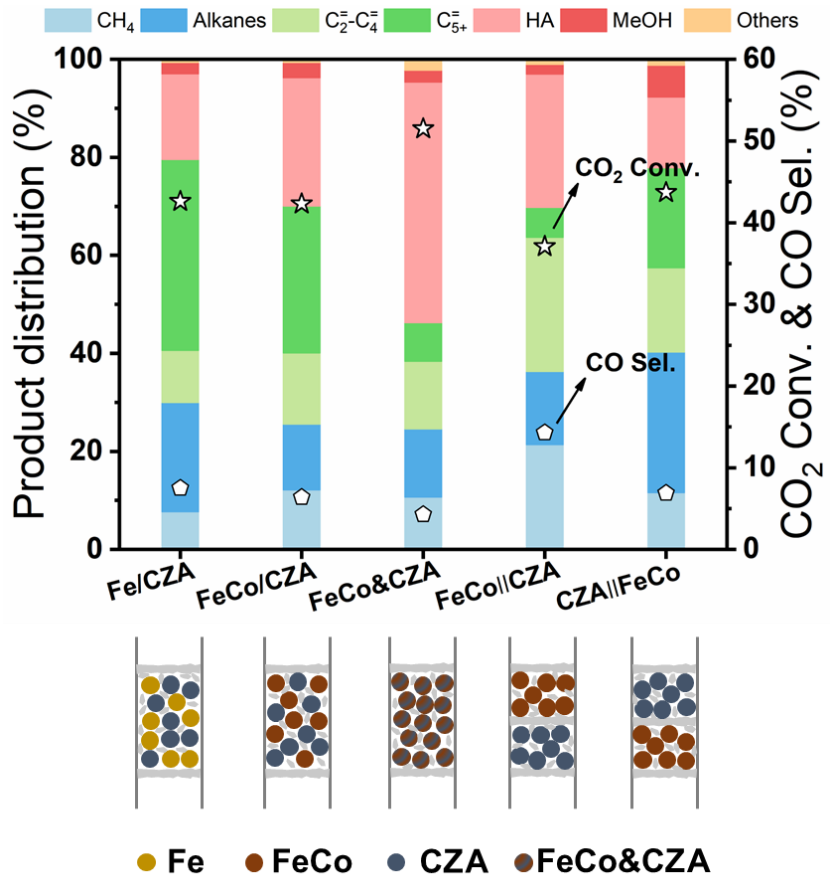

Supplementary Fig. 5. The reaction performance of the multifunctional catalysts with different mixing manners. Fe/CZA and FeCo/CZA represent the particle mixing modes, FeCo&CZA represents the powder mixing mode, and Fe||CZA and FeCo||CZA represent the dual-bed modes. Reaction conditions: 320°C, 5.0 MPa, $H_2/CO_2 = 3$, multifunctional catalyst consists of Fe-based catalyst of 0.1 g and CZA of 0.1 g, TOS = 8 hours, 4500 ml g_{cat}^{-1} h^{-1}.
Note: Fe/CZA exhibited low $C_{2+}OH$ selectivity of 17.5% at a CO_2 conversion of 42.6%. For the dual-bed mode of CZA||FeCo, more methanol (6.5%) was obtained due to that CZA at the above layer led to the preferential formation of methanol. More CO (14.3%) was formed from FeCo||CZA case due to the suppressed mass transfer effect and sluggish CO consumption.

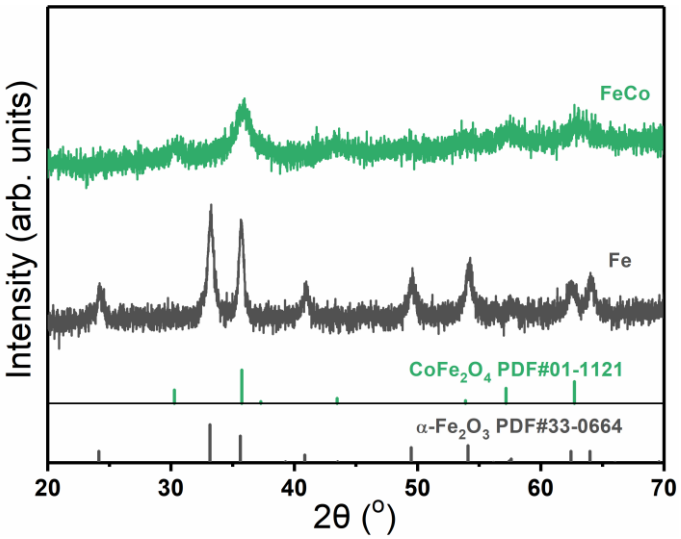

Supplementary Fig. 6. The crystal structure analysis of fresh catalysts. XRD patterns of the fresh FeCo and Fe catalysts.

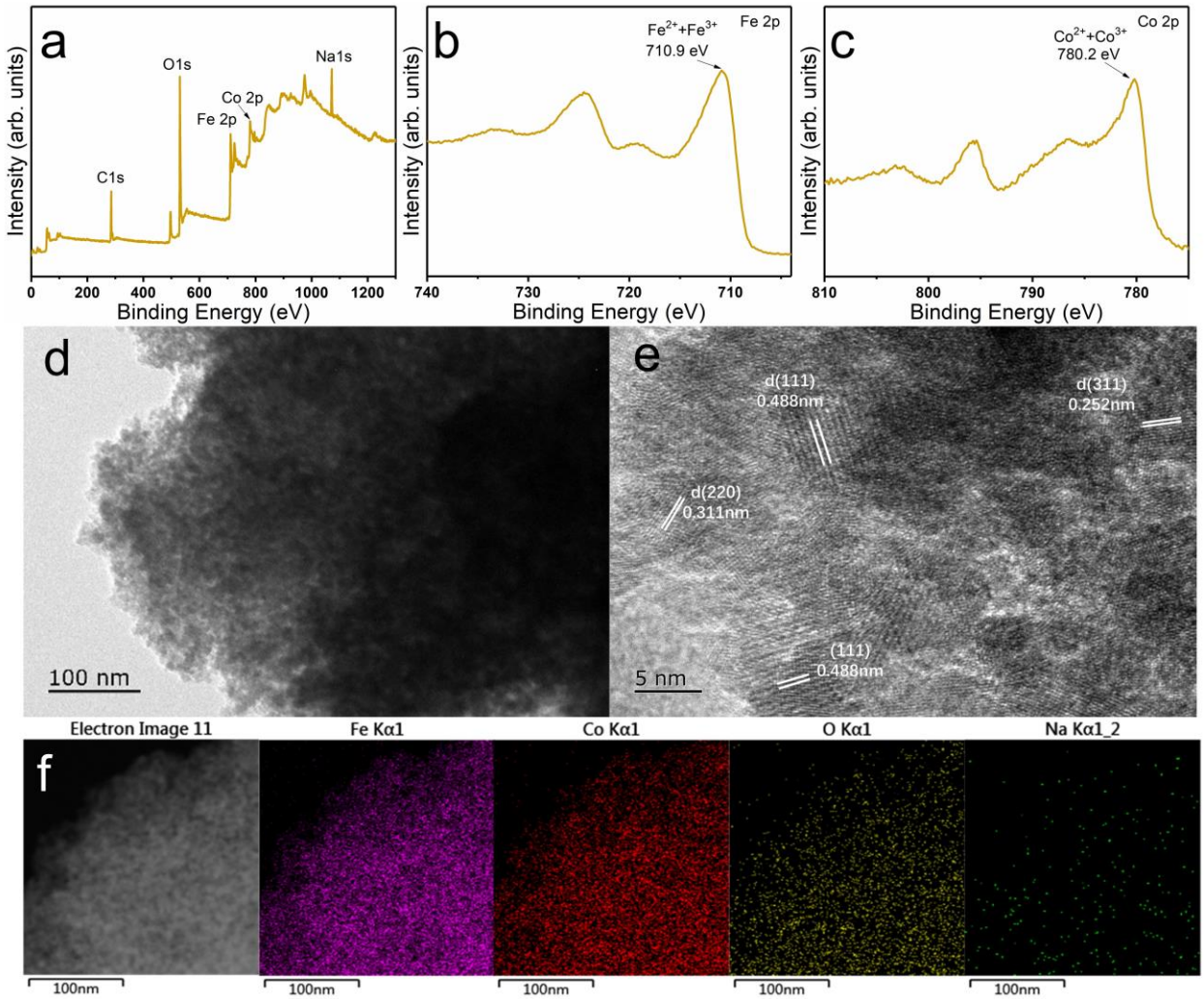

Supplementary Fig. 7. The structure analysis of fresh FeCo catalyst. (a-c) XPS spectra, (d-e) TEM images, and (f) TEM mapping images of fresh FeCo catalyst.

Note: The XRD patterns of the fresh FeCo and Fe catalysts are exhibited in Supplementary Fig. 6. The typical diffraction peaks of FeCo and Fe catalysts overlapped with that of the references FeCo alloy oxide and α-Fe_2O_3 (PDF #33-0664), respectively. The elements of Fe, Co, O, and Na in the fresh FeCo catalyst were detected by XPS (Supplementary Fig. 7a). The Fe2*p* and Co2*p* spectra were consistent with the FeCo alloy oxide (Supplementary Figs. 7b and c)[25]. The fresh FeCo catalyst was composed of nanoparticles as shown in the TEM image of Supplementary Fig. 7d. The obvious lattice fringes of 0.488 nm, 0.311nm, and 0.252nm measured in HRTEM images (Supplementary Fig. 7e) corresponded to the 111, 220, and 311 planes of the FeCo alloy oxide crystal. As shown in the TEM mapping images (Supplementary Fig. 7f), the elements of Fe, Co, O, and Na were evenly distributed on the fresh FeCo catalyst.

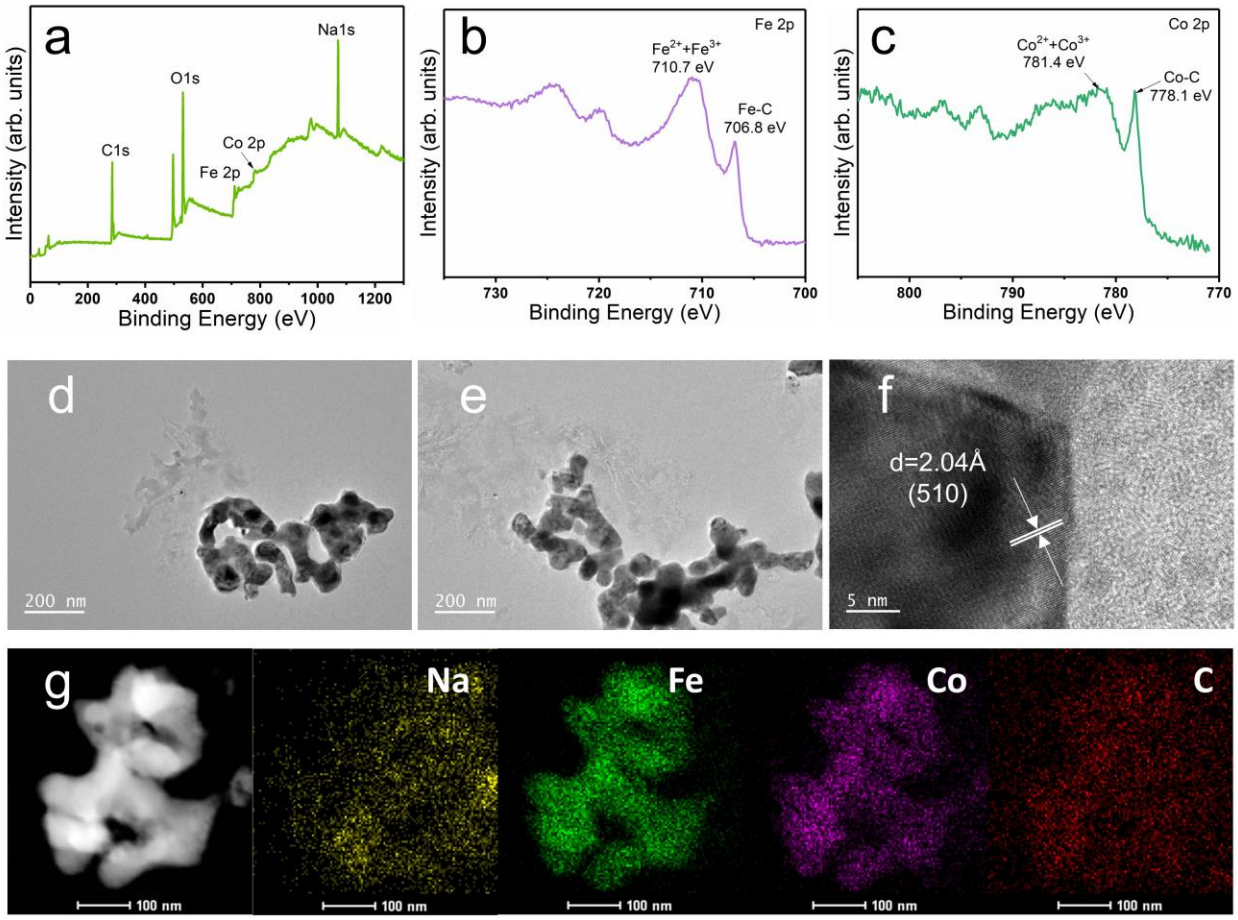

Supplementary Fig. 8. The structure analysis of spent FeCo alloy carbide catalyst. (a-c) XPS spectra, (d-f) TEM images, and (g) TEM mapping images of spent FeCo alloy carbide catalyst.

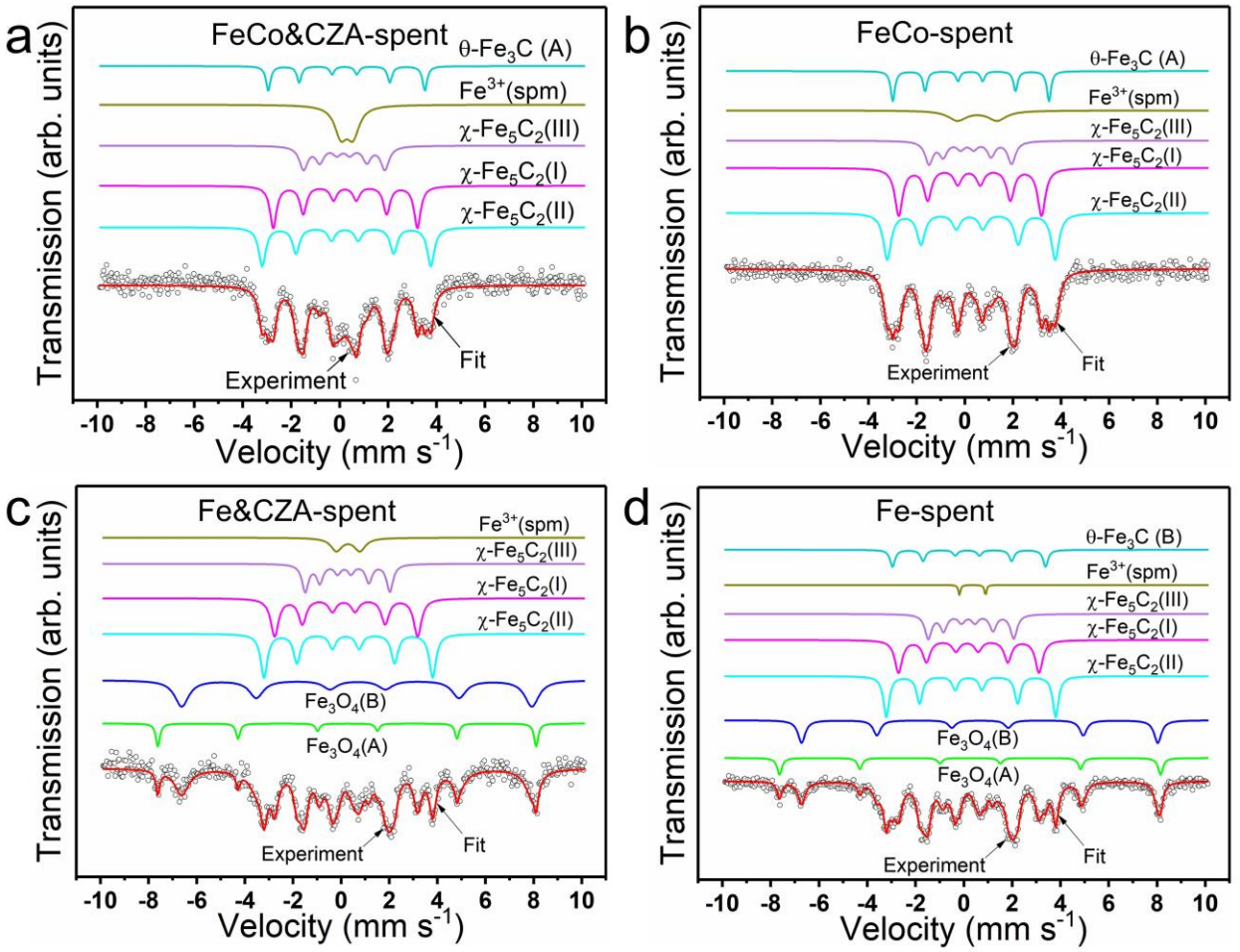

Supplementary Fig. 9. The fine analysis of Fe components in series catalysts. ^{57}Fe Mössbauer spectra of (a) FeCo&CZA-spent, (b) FeCo-spent, (c) Fe&CZA-spent, and (d) Fe-spent catalysts. **Note:** Different components (χ-Fe_5C_2, Fe_3O_4, Fe^{3+}, or θ-Fe_3C) were fitted from the ^{57}Fe Mössbauer spectra of the spent catalysts (FeCo&CZA-spent, FeCo-spent, Fe&CZA-spent, and Fe-spent), and the detailed parameters are listed in Supplementary Table 6. Generally, FeCo alloy carbide was the major phase in the FeCo&CZA-spent and FeCo-spent catalysts, accounting to 72.1% and 80.7%, respectively. On the contrary, Fe_3O_4 appeared in the Fe&CZA-spent and Fe-spent catalysts in addition to carbide phases, which is consistent with the XRD results. Especially, more Fe_3O_4 (35.6%) was detected in the Fe&CZA-spent compared with that in the Fe-spent catalyst, mostly because of the increased oxidant of H_2O from the CZA-catalyzed RWGS reaction ($CO_2 + H_2 \rightarrow CO + H_2O$). Therefore, the absence of Fe_3O_4 in FeCo&CZA-spent and FeCo-spent implies that a superior anti-oxidation property of the Co-containing catalysts. The tailored oxophilicity of FeCo carbide in turn affects the surface adsorption of reaction intermediates, and helps to boost the $C_{2+}OH$ synthesis performance.

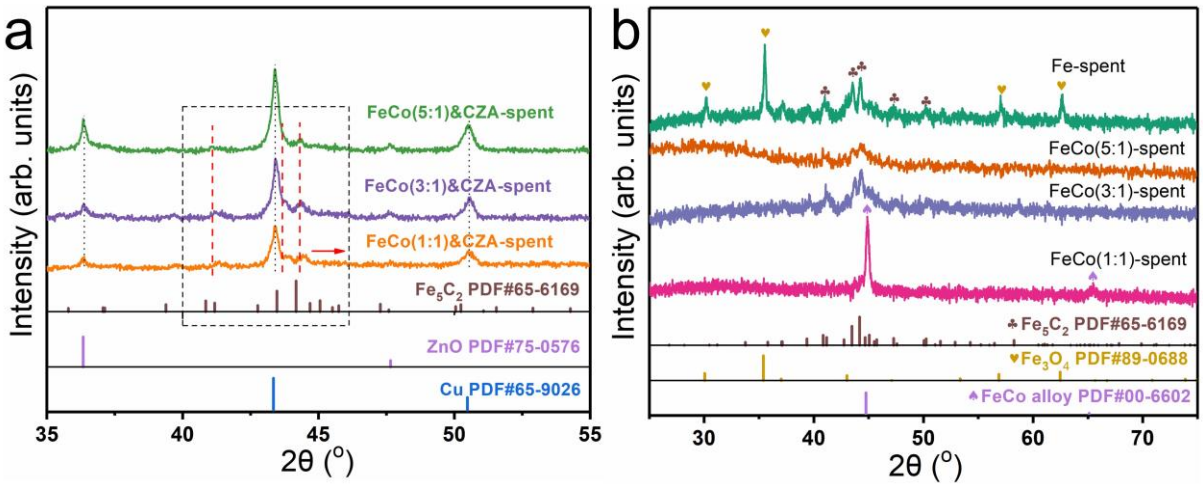

Supplementary Fig. 10. The structure analysis of series spent FeCo&CZA catalysts. XRD patterns of (a) FeCo&CZA-spent catalysts with different ratios of Fe/Co, and (b) Fe-spent catalyst and FeCo-spent catalysts with different ratios of Fe/Co.

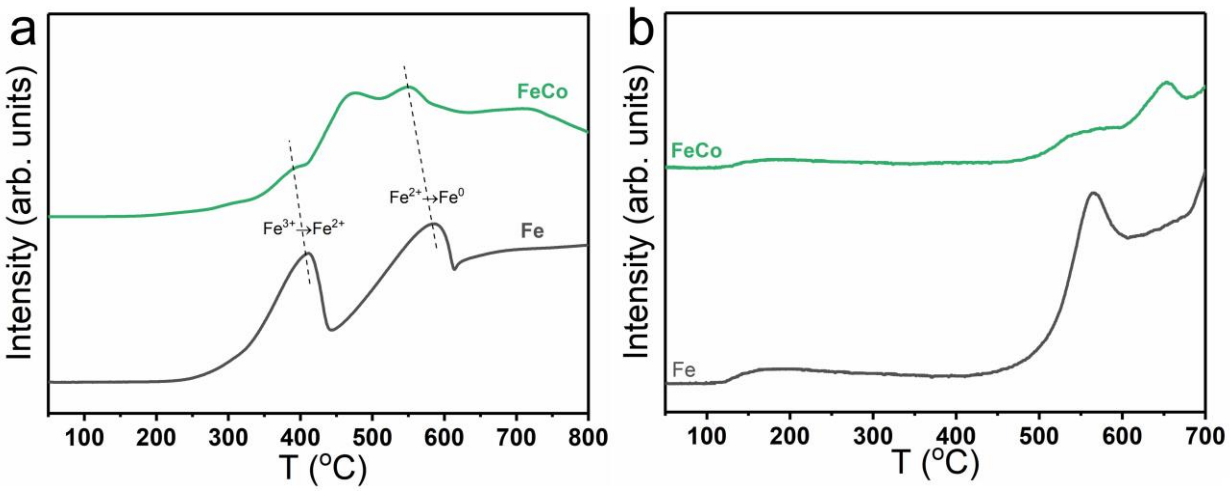

Supplementary Fig. 11. The structural evolution analysis of the Fe-based catalysts. The (a) H_2-TPR and (b) CO-TPD of FeCo and Fe catalysts.

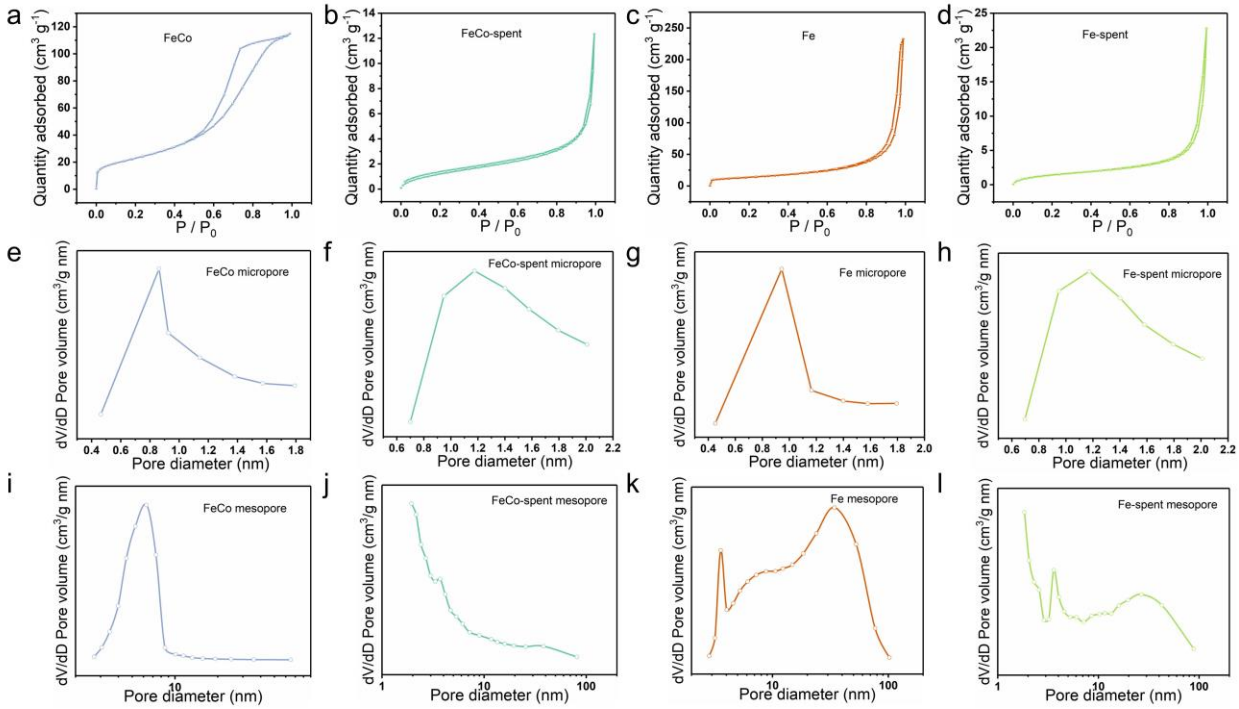

Supplementary Fig. 12. The specific surface area and pore structure analysis of Fe-based catalysts. N_2 adsorption-desorption isotherm of (a) FeCo, (b) FeCo-spent, (c) Fe, and (d) Fe-spent catalysts as well as their (e-l) pore size distribution.

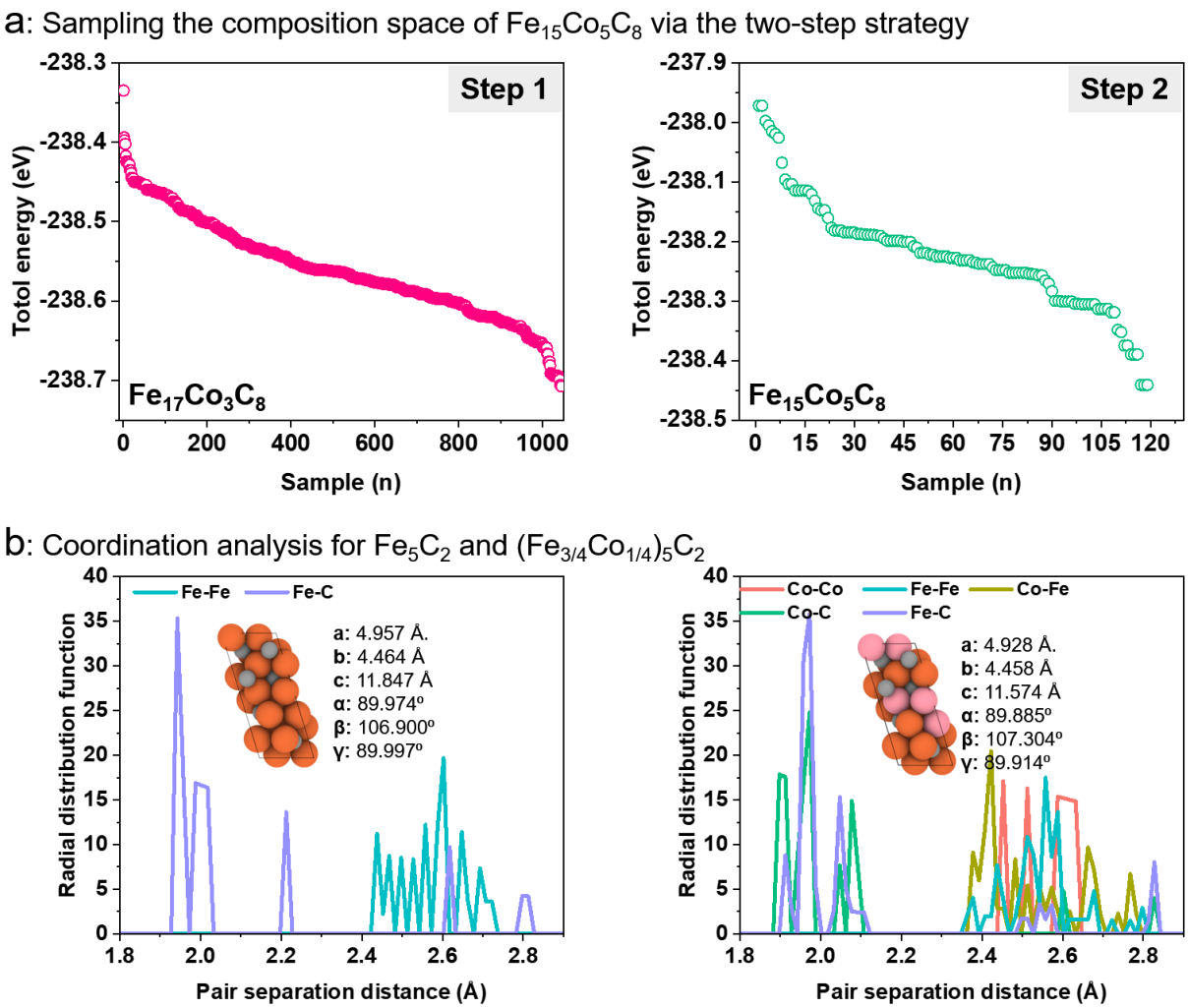

Supplementary Fig. 13. DFT-driven compositional composition screening and structural analysis. (a) Energy distribution of 1140 $Fe_{17}Co_3C_8$ and 120 $Fe_{15}Co_5C_8$ crystal configurations. (b) Radial distribution analysis (RDF) of different bonds in the stable crystal phase of Fe_5C_2 and $(Fe_{3/4}Co_{1/4})_5C_2$. The optimized structures and the corresponding lattice parameters are shown in the insets.

Note: $(Fe_{3/4}Co_{1/4})_5C_2$ possesses a similar crystal phase to the Fe_5C_2, but the exact structure including the atom distribution in the crystal has not been identified in theory. To realize the possible structure of $(Fe_{3/4}Co_{1/4})_5C_2$ with the Fe/Co molar ratio of 3, it is necessary to substitute five Fe atoms in the Fe_5C_2 lattice to the Co atoms. However, the unit cell of Fe_5C_2 contains 20 Fe and 8 C atoms, once substitution is carried out, 15504 possible combinations among 15 Fe and 5 Co atoms (without excluding duplicates) could exist. To minimize the computational cost, we proposed a two-step strategy to narrow the sampling space and to identify the ground structure of $(Fe_{3/4}Co_{1/4})_5C_2$. First, we sampled all the possible structures of $Fe_{17}Co_3C_8$ with less Co content by creating 1140 structure models, and optimized the structure to obtain their electronic energies (Step 1, Supplementary Fig. 13a). Then, we selected ten candidate materials with low electronic energies for the following substitution, which yields 120 $Fe_{15}Co_5C_8$ (i.e., $(Fe_{3/4}Co_{1/4})_5C_2$) structures (Step 2, Supplementary Fig. 13a). Finally, the most stable configuration of $Fe_{15}Co_5C_8$ with the most

negative electronic energy was obtained and used for further analysis. Geometrically, the identified $(Fe_{3/4}Co_{1/4})_5C_2$ has a smaller lattice than the Fe_5C_2 (Supplementary Fig. 13), in terms of the lattice contraction effect as shown in the XRD patterns (Fig. 2a). Radical distribution function (RDF) analysis indicated that the reduced lattice parameters was mainly due to the decreased bond length of Fe-C. As shown in Supplementary Fig. 13b, the Fe-C bond lengths were well above 1.91 Å on the Fe_5C_2 model, and the major peaks of Fe-C bonds were located at 1.95, 2.21, 2.61, and 2.80 Å. However, on the $(Fe_{3/4}Co_{1/4})_5C_2$ model, almost all the peaks of Fe-C shifted toward the smaller values. For example, the original peak of Fe-C at 2.21 Å shifted to 2.06 Å, and the peak near 1.95 Å was rearranged, which formed a new peak at 1.91 Å. The newly formed Co-C bonds were slightly shorter than the Fe-C bonds as indicated by the formation of a new peak at 1.90 Å, and the Co-Fe bonds were generally shorter than the Co-Co and Fe-Fe bonds.

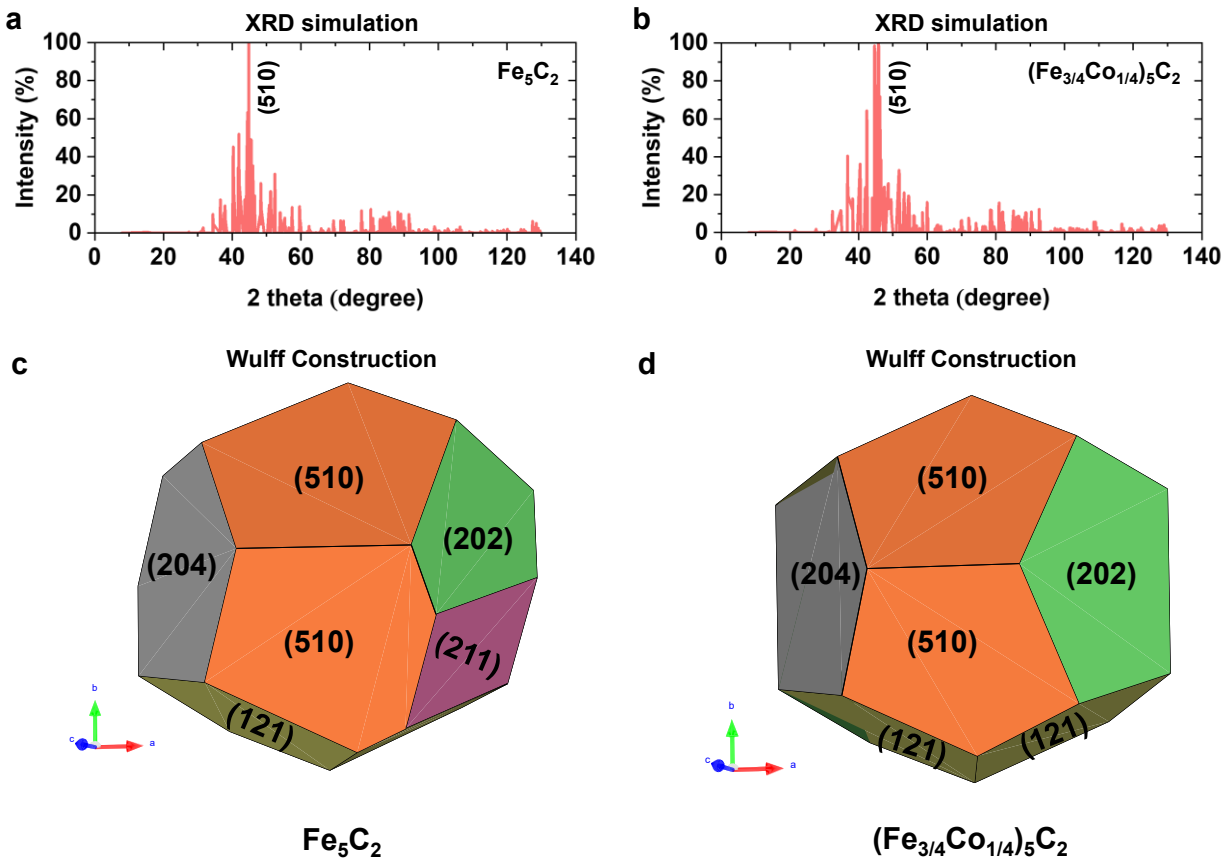

Supplementary Fig. 14. Simulated X-Ray Diffraction and Wolf Surface Construction. Simulated XRD (a and b) and constructed equilibrium structures (c and d) base on the Wulff construction of Fe_5C_2 and $(Fe_{3/4}Co_{1/4})_5C_2$.

Note: We simulated the XRD of Fe_5C_2 and $(Fe_{3/4}Co_{1/4})_5C_2$ using the theoretical identified crystal models. We found that these two crystals have the similar XRD peaks with dominated (510) peak below 45 degrees. However, $Fe_{3/4}Co_{1/4})_5C_2$ generally shows the higher angles than the Fe_5C_2, similar to the experimental XRD results of Fe carbide and FeCo carbide (Fig. 2a). On the basis of the XRD results, we then employed the Wulff construction to predict the equilibrium shape of Fe_5C_2 and $(Fe_{3/4}Co_{1/4})_5C_2$ crystallite by selecting top twenty high intensity peaks (Supplementary Fig. 14b). The results indicated that (510) face holds the largest part in both Fe_5C_2 and $(Fe_{3/4}Co_{1/4})_5C_2$.

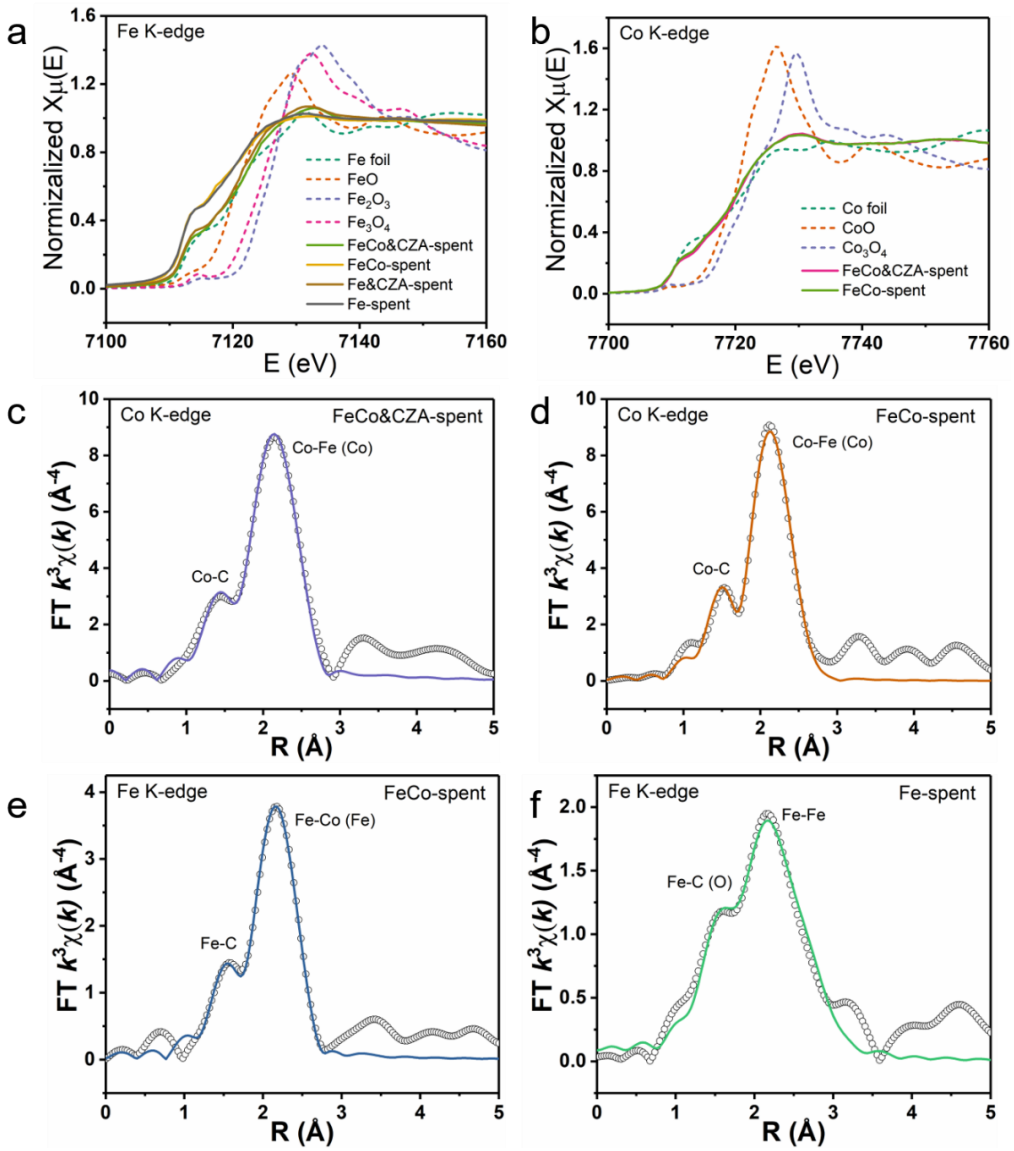

Supplementary Fig. 15. The fine structure of series catalysts. (a) Normalized Fe K-edge XANES spectra of the FeCo&CZA-spent, FeCo-spent, Fe&CZA-spent, and Fe-spent catalysts after CO_2 hydrogenation reaction in reference to the Fe foil, FeO, Fe_2O_3, and Fe_3O_4. (b) Normalized Co K-edge XANES spectra of the FeCo&CZA-spent and FeCo-spent catalysts after CO_2 hydrogenation reaction in reference to the Co foil, CoO, and Co_3O_4. (c-f) Fourier transforms (FT) of the k^3-weighted EXAFS spectra (circles) and fitted curves (solid lines) of the spent catalysts at the Co K-edge (c, d) and Fe K-edge (e, f).

Note: The X-ray absorption near-edge structure (XANES) and extended X-ray absorption fine structure (EXAFS) experiments were performed to reveal the coordination environment of Fe and Co species in the spent catalysts (Supplementary Fig. 15). Fe-C and Co-C bonds were both confirmed in the FeCo&CZA-spent and FeCo-spent catalysts (Supplementary Tables 8 and 9). The Fe-Fe (Co) bond length in the FeCo&CZA-spent catalyst (2.57 Å) was slightly shorter than that of the Fe&CZA-spent catalyst (2.64 Å), suggesting the lattice contraction effect in FeCo alloy carbide, which agrees well with the XRD and DFT results (Fig. 2a and Supplementary Fig. 13).

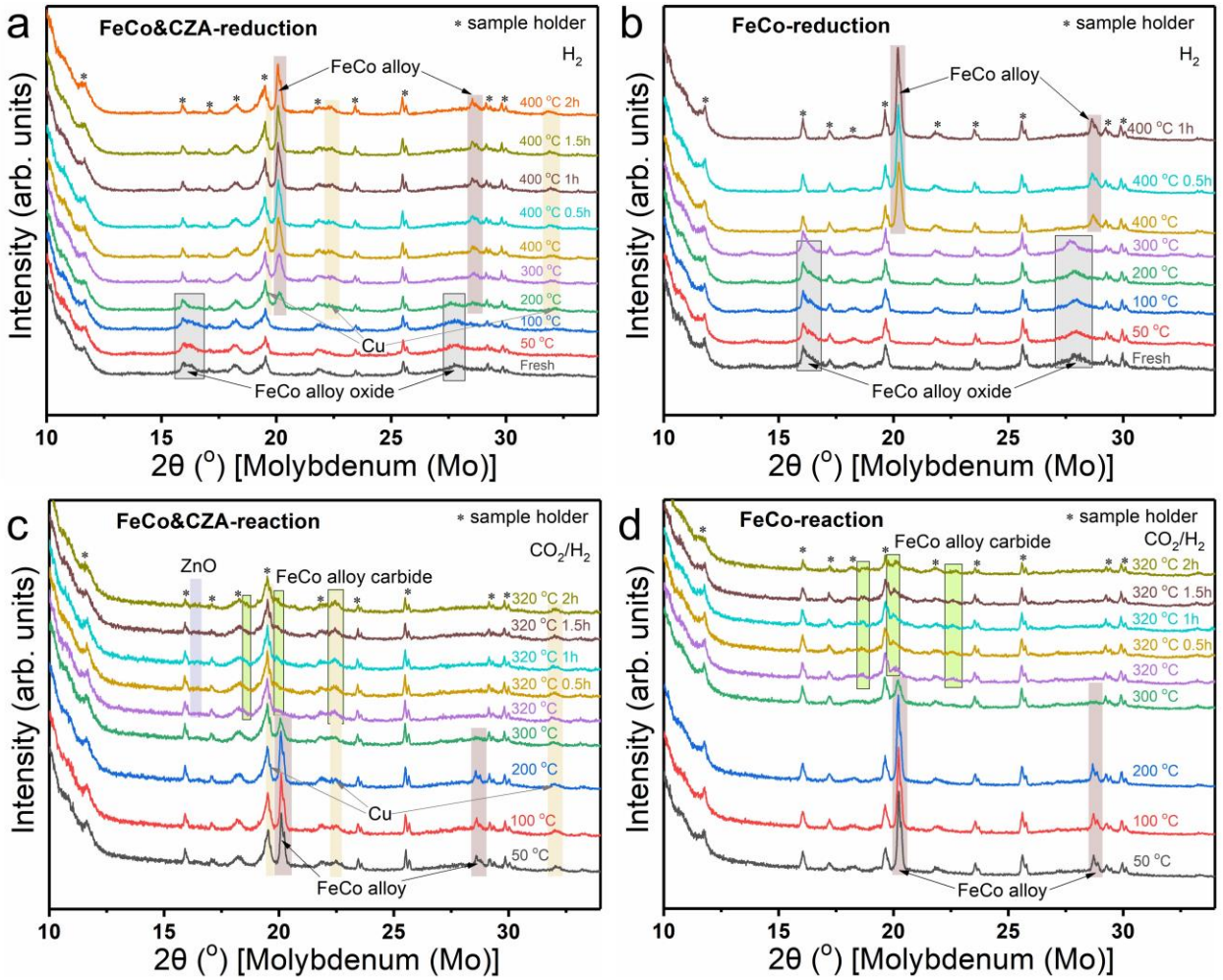

Supplementary Fig. 16. The structure analysis of series catalysts during reduction and reaction process. The in-situ XRD patterns of (a) FeCo&CZA reduction, (b) FeCo reduction, (c) FeCo&CZA reaction, and (d) FeCo reaction with Mo Kα radiation. "*" symbol represents the diffraction peaks of sample holder, which is unavoidable because of supporting the samples.

Note: The phase evolution behaviors of FeCo&CZA and FeCo catalysts were monitored by in-situ XRD under H_2 reduction (atmospheric pressure and temperature increased from room temperature to 400 °C) and CO_2 hydrogenation (3 MPa and temperature increased from 50 to 320 °C) conditions. In order to allow the X-ray to penetrate the in-situ high-pressure reaction cell, a molybdenum target (Mo Kα radiation) was used for the tests. Similar to the ex-situ XRD results, FeCo alloy oxide was also detected in the in-situ XRD patterns of the fresh FeCo&CZA (Supplementary Fig. 16a). During the H_2 reduction process, FeCo alloy and Cu phases appeared at 200 °C in the FeCo&CZA catalyst, which is earlier than that in the FeCo catalyst (400 °C) (Supplementary Fig. 16b). These results suggest that the CZA facilitated H_2 dissociation and promoted the reduction of the metallic oxide components. During the CO_2 hydrogenation reaction (Supplementary Fig. 16c), the FeCo alloy disappeared at 320 °C, and FeCo alloy carbide and ZnO phases appeared with the extension of reaction time under 320 °C. The FeCo catalyst had same phase evolution phenomena during the CO_2 hydrogenation reaction (Supplementary Fig. 16d).

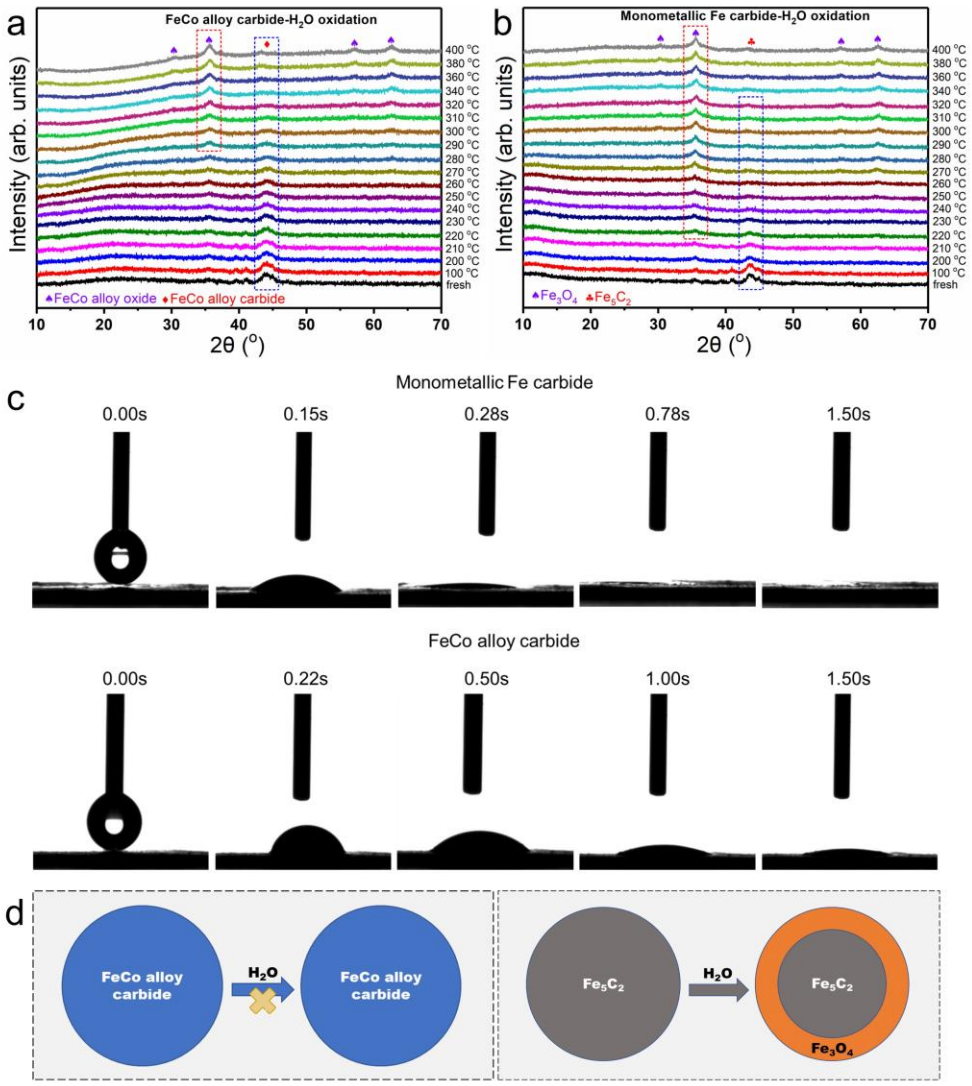

Supplementary Fig. 17. The water oxidation analysis of Fe carbide and FeCo alloy carbides. (a-b) In-situ XRD patterns of water oxidation on FeCo alloy carbide (a) and monometallic Fe carbide (b) with Cu Kα radiation. (c) Water contact angles test of monometallic Fe carbide and FeCo alloy carbide. (d) Schematic illustration of the phase evolution in FeCo alloy carbide and monometallic Fe carbide under the water-rich atmosphere. FeCo alloy carbide and monometallic Fe carbide with pure phase were prepared by CO carburization method.

Note: The in-situ water oxidation XRD experiment was performed to evaluate the anti-oxidation property of the FeCo alloy carbide and monometallic Fe carbide under the water-rich atmosphere. Until the temperature as high as 400 ^{o}C, the carbide crystal phase was still maintained in FeCo alloy carbide (Supplementary Fig. 17a). However, the carbide phase disappeared in the monometallic Fe carbide catalyst when the temperature reached 320 ^{o}C (Supplementary Fig. 17b), suggesting that the oxidation of monometallic Fe carbide catalyst by water occurs more easily. In addition, FeCo alloy carbide was more hydrophobic as confirmed by the water contact angle test (Supplementary Fig. 17c). Therefore, the strong anti-oxidation property of the FeCo alloy carbide can well maintain its surface configuration under the reaction conditions which guaranteed the excellent catalytic stability and unique targeted products selectivity.

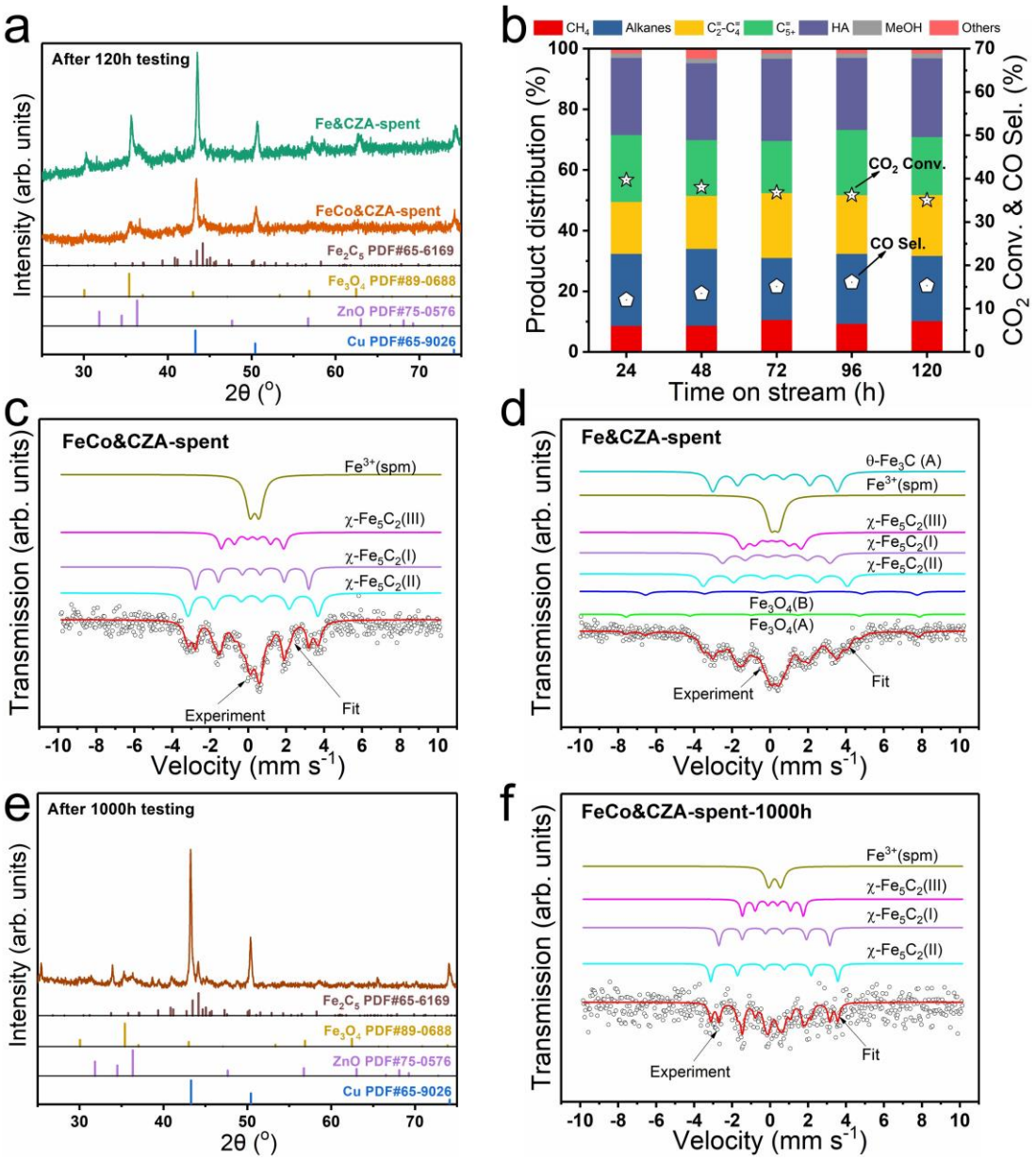

Supplementary Fig. 18. The catalytic performance and its catalysts of structure analysis after 120 h reaction. (a) XRD patterns, (b) the catalytic performance of Fe&CZA catalyst, (c and d) ^{57}Fe Mössbauer spectra of catalysts after 120 hours stability test. Reaction conditions: 320°C, 5.0 MPa, H_2/CO_2 = 3, multifunctional catalyst consists of Fe-based catalyst of 0.1 g and CZA of 0.1 g, 4500 ml g_{cat}^{-1} h^{-1}. (e) XRD patterns and (f) ^{57}Fe Mössbauer spectra of catalysts after 1000 hours stability test.

Note: The crystal structure of spent catalysts after reaction was analyzed by ^{57}Fe Mössbauer spectra (Supplementary Table 10) and XRD. Considerable Fe_3O_4 phase were detected in Fe&CZA-spent, but no clear oxidates were formed in the FeCo&CZA-spent. These results indicate that the formation of FeCo carbide can effectively suppress the oxidation and avoid the in-situ generation of Fe_3O_4 phase.

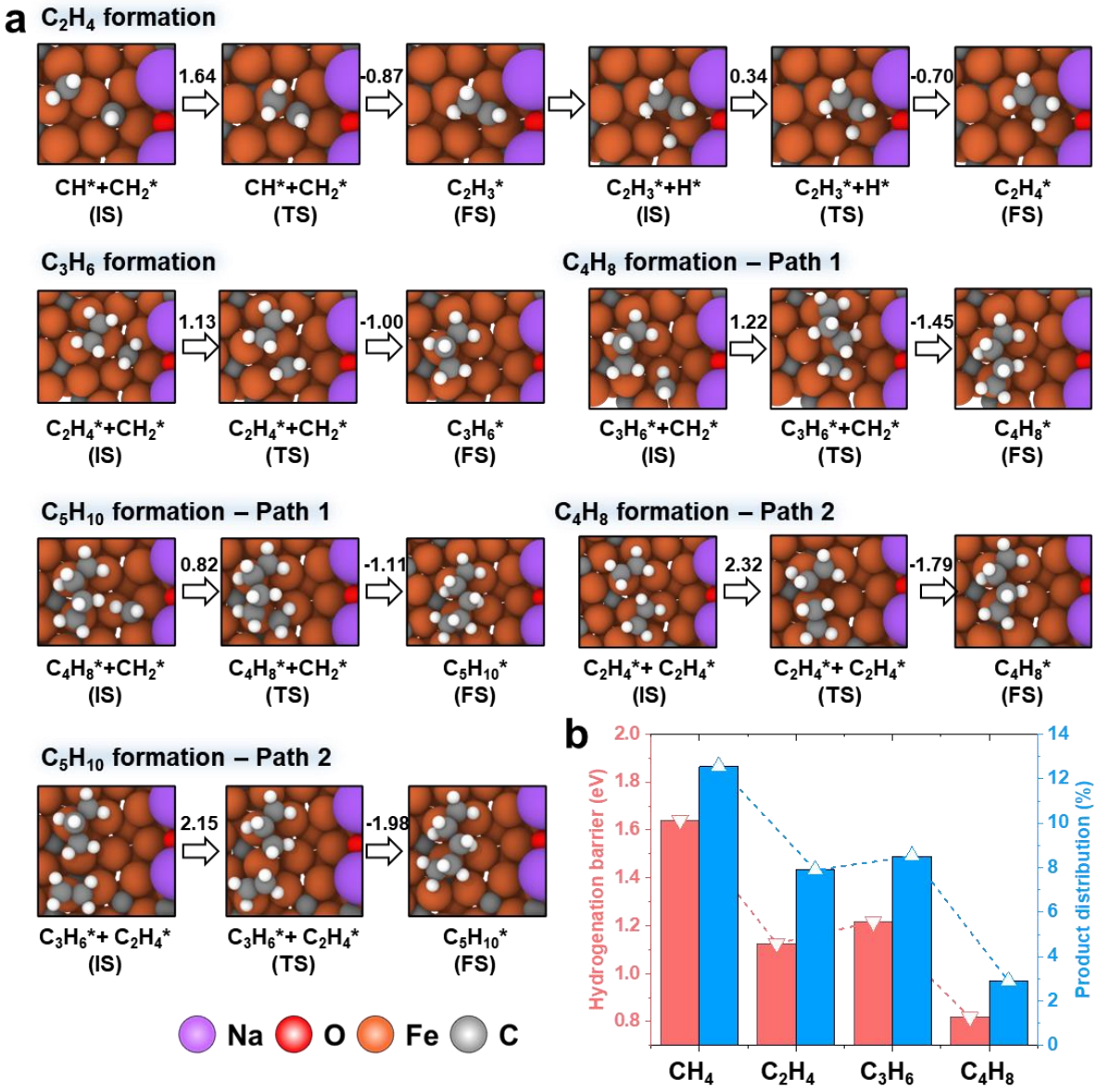

Supplementary Fig. 19. Transition State Identification in Hydrocarbon Production Pathways. (a) The energy favorable reaction pathways for generation of multiple hydrocarbons on $Fe_5C_2(510)$. (b) The relationship between the conversion barriers of different hydrocarbons and experimental products distribution.

Note:

Identification of active surface:

To verify the key active surface for CO_2 hydrogenation, we selected the $Fe_5C_2(510)$ surface as a prototype to reveal the products distribution of hydrocarbons observed in experiments. Noteworthy that we demonstrated that $Fe_5C_2(510)$ surface prefers to generate hydrocarbons via the CH_x* species (Fig. 3b), we therefore investigated here all the possible couplings between two different CH_x* (x= 1, 2, and 3) species for generation of C_2 to C_5 alkenes, and only the energy favorable pathways are shown in Supplementary Fig. 19a. We found the C_2H_4 is mainly generated by firstly

coupling of CH* with CH_2* with an energy barrier of 1.63 eV. Once C_2H_3* is formed, the C_2H_4 can be obtained by the subsequent hydrogenation step with an energy barrier of 0.34 eV. After the generation of C_2H_4*, two possible routes could exist besides the desorption, including 1) the further hydrogenation into C_2H_6 via the C_2H_5 species, and 2) the subsequent interaction with the other CH_2* that forms the C_3H_6 product. Our computations indicated that the further hydrogenation into C_2H_6 is energy unfavorable than the formation of C_3H_6 product. The computed energy barriers for these two pathways are 1.27 and 1.13 eV respectively, suggesting the Fe_5C_2(510) prefers to catalyze the alkene than the alkane. Therefore, we then focused on the generation of alkenes instead of alkanes in the subsequent investigations.

Following the above procedure, we conducted the further formation of C_4 to C_5 products by considering different combinations. For example, we evaluated the formation of C_4H_8* via the couplings between the C_3H_6* and CH_2*, and two C_2H_4*. We found the multi-carbons (C_4 and C_5 alkenes) are mainly formed via the CH_2* medium with smaller energy barriers. On the basis of these energy barriers, we can assess the product ratio in the CO_2 hydrogenation process. Generally, a larger conversion barrier than the formation barrier for a chemical can yield a larger ratio in the product spaces. For example, we found that the formation of CH_4 (1.23 eV on Site 1, and 1.48 eV on Site 2) has a lower energy barrier than that of the formation of C_2H_4 (1.64 eV). This leads to a larger ratio of CH_4 than the C_2H_4. In similar, if we compare the formation of C_2H_4 and the conversion of C_2H_4 into C_3H_6, we can find that the C_3H_6 generation has a large energy barrier (1.22 eV vs. 1.13 eV) which implies that C_2H_4 could holds a larger proportion than the C_3H_6. Exactly, we plotted the energy barriers with the experimentally realized product ratios, and found a high correlation (Supplementary Fig. 19b), which suggests that the Fe_5C_2(510) could be the major active surface for the CO_2 hydrogenation in this study. Therefore, the (510) crystal face was employed for DFT computations.

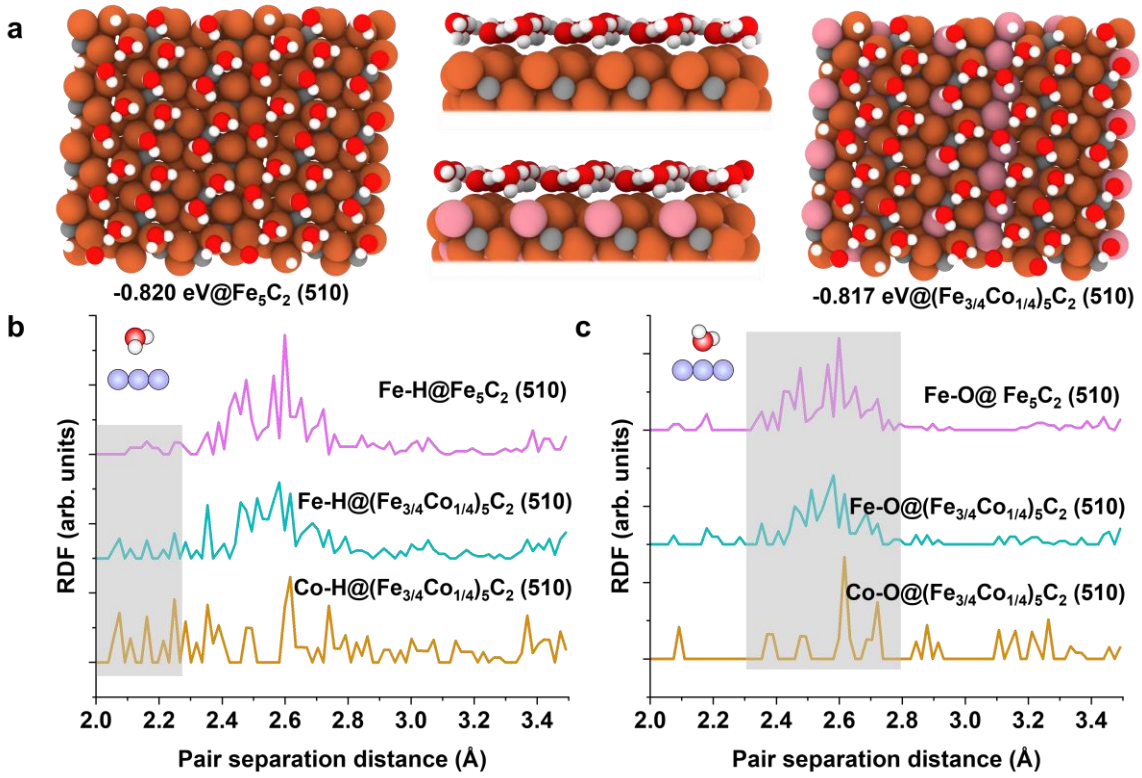

Supplementary Fig. 20. Water adsorption and RDF analysis. (a) Top and side views of water adsorption on Fe_5C_2(510) and $(Fe_{3/4}Co_{1/4})_5C_2$(510) surfaces at the coverage of one monolayer. Radial distribution function (RDF) for water adsorption as the function of metal-hydrogen (b) and metal-oxygen (c) distances.

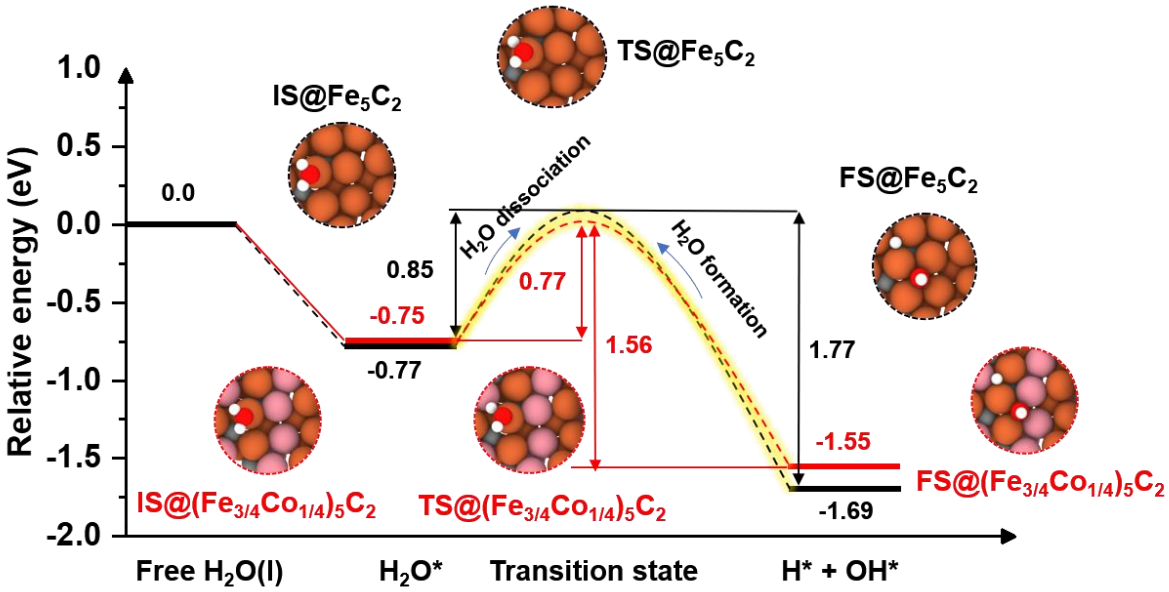

Supplementary Fig. 21. Water dissociation and formation. Energy profiles of the water dissociation/formation on the $Fe_5C_2(510)$ and $(Fe_{3/4}Co_{1/4})_5C_2(510)$ surfaces. The initial states (IS), transition states (TS), and final states (FS) are shown in the insets.

Note: The different responses of $Fe_5C_2(510)$ and $(Fe_{3/4}Co_{1/4})_5C_2(510)$ to the H_2O oxidation were investigated by two aspects, including H_2O adsorption (Supplementary Fig. 20) and H_2O dissociation/formation (Supplementary Fig. 21). First, we studied H_2O adsorption on the two catalytic surfaces at different coverages (i.e., single molecule adsorption and one monolayer adsorption). At low coverage, both of the two surfaces preferred to adsorb water via the Fe sites, and the adsorption of water molecules onto the Co sites in the $(Fe_{3/4}Co_{1/4})_5C_2(510)$ was mostly suppressed, as indicated by a spontaneous diffusion from the Co sites to the neighboring Fe sites during adsorption relaxation. Specifically, by comparison with the pristine structure of $Fe_5C_2(510)$, the introduction of Co into the Fe_5C_2 lattice weakened the H_2O adsorption energy by 0.02 eV from -0.77 eV on $Fe_5C_2(510)$ to -0.75 eV on $(Fe_{3/4}Co_{1/4})_5C_2(510)$ (see Supplementary Fig. 21). With the increase of water coverage up to one monolayer, water molecules could form a water network on the catalytic surface and stabilize the overall systems through the H-bonds (Supplementary Fig. 20a). The average adsorption energy difference between $Fe_5C_2(510)$ and $(Fe_{3/4}Co_{1/4})_5C_2(510)$ was decreased to 0.003 eV. But differently, RDF analysis found a clear H-oriented adsorption behavior on the Co sites (Supplementary Fig. 20b), whereas the Fe atoms in both models tended to interact with water via the O atoms, suggesting a stronger oxophilicity of Fe than Co sites. These results could explain why FeCo catalysts developed in this work showed slower response to water during the water contact angles test (Supplementary Fig. 17c).

Upon water adsorption, dissociation may occur, and the different binding strengths between the O-containing species and the catalysts might affect the catalytic performance. Thus, we then investigated the water dissociation kinetics using the climbing image nudged elastic band (CI-NEB) method (Supplementary Fig. 21). Our computations indicated that the water dissociation on both $(Fe_{3/4}Co_{1/4})_5C_2(510)$ and $Fe_5C_2(510)$ were facile with the energy barrier of 0.77 and 0.85 eV, respectively. However, once dissociated, OH* was found to bind more strongly to the $Fe_5C_2(510)$ than to the $(Fe_{3/4}Co_{1/4})_5C_2(510)$, resulting in a larger barrier of the surface reduction [$OH^* + H^* \rightarrow H_2O^*$, 1.77 eV on $Fe_5C_2(510)$ *vs.* 1.56 eV on $(Fe_{3/4}Co_{1/4})_5C_2(510)$]. Therefore, under the

reaction conditions, the large barrier of the OH* reduction on the $Fe_5C_2(510)$ would suppress the formation of water molecules, leading to the further transformation of OH* into O* occurs that poisons the carbide active sites.

Indeed, binding energy of O* on the $Fe_5C_2(510)$ was estimated to be -3.50 eV, 0.36 eV higher than that on the $(Fe_{3/4}Co_{1/4})_5C_2(510)$. In particular, under the high coverage of oxygen atoms, the average binding energy difference remained at 0.15 eV (see Fig. 2f), indicating the stronger oxophilicity of $Fe_5C_2(510)$. These results agreed well with our TPO-MS analysis, where the monometallic Fe carbide tended to be oxidized at lower temperature than the FeCo alloy carbide (Fig. 2e), suggesting that the improved oxidation resistance of the FeCo alloy carbide is strongly associated with the capability for the O transformation (i.e., water formation, surface coupling between O atoms, or O with other species such as C).

To further understand the different oxophilicity of $Fe_5C_2(510)$ and $(Fe_{3/4}Co_{1/4})_5C_2(510)$, we finally computed the crystal orbital Hamilton populations (COHP) for the O adsorption (Fig. 2g). We found that the O readily interacted with the models via 2*p*-3*d* orbital hybridization, forming two bonding states near the -20.0 eV and -6.0 eV, and antibonding states above -5.0 eV. Integration of COHP up to the Fermi level could quantify the binding strength between the O and the catalysts. By definition, a more negative value of integrated COHP (ICOHP) indicated a stronger binding. The larger value of ICOHP on the $Fe_5C_2(510)$ (-7.75 eV) than the $(Fe_{3/4}Co_{1/4})_5C_2(510)$ (-7.61 eV) indicated that the $Fe_5C_2(510)$ possessed a stronger oxophilicity than $(Fe_{3/4}Co_{1/4})_5C_2(510)$, which is consistent with our binding energy analysis.

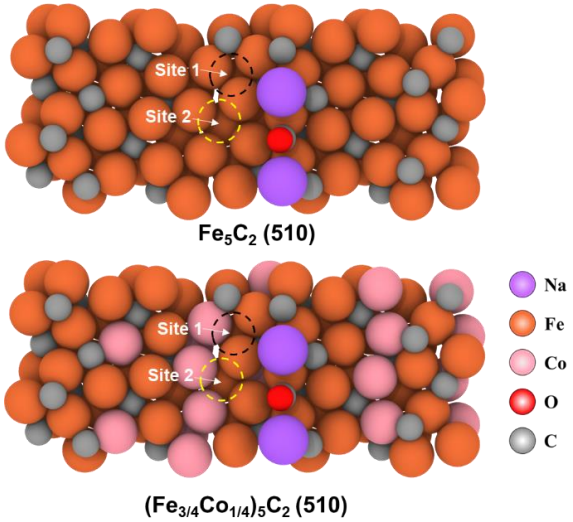

Supplementary Fig. 22. The full configuration of Fe_5C_2(510) and $(Fe_{3/4}Co_{1/4})_5C_2$(510) models. Two reaction sites including Site1 and Site 2 were selected for the reaction kinetic analysis. **Note:** In these two catalytic models, Na_2O was anchored on the Fe_5C_2(510) and $(Fe_{3/4}Co_{1/4})_5C_2$(510) surfaces to simulate the real catalytic interfaces that used in CO_2 hydrogenation. We assumed that the catalytic interfaces are partially reduced that contain both unsaturated Fe or Co sites near the Na_2O for the reaction. The saturated sites are covered by the C atoms.

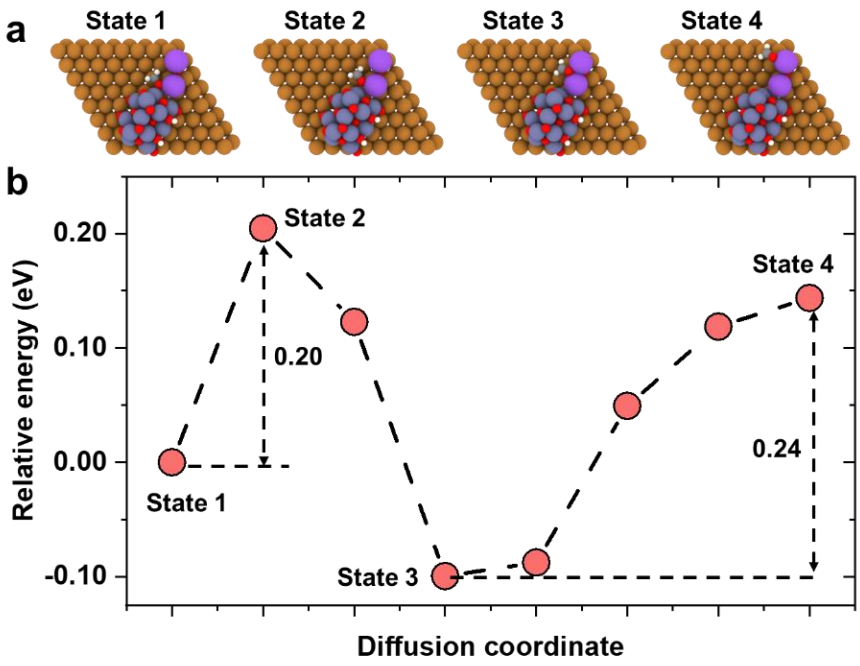

Supplementary Fig. 23. The diffusion/spillover pathways of CH_2O* on the interface of K_2O/Cu(111)/ZnO(101). (a) Key reaction states. (b) Relative energy change along the reaction pathway.

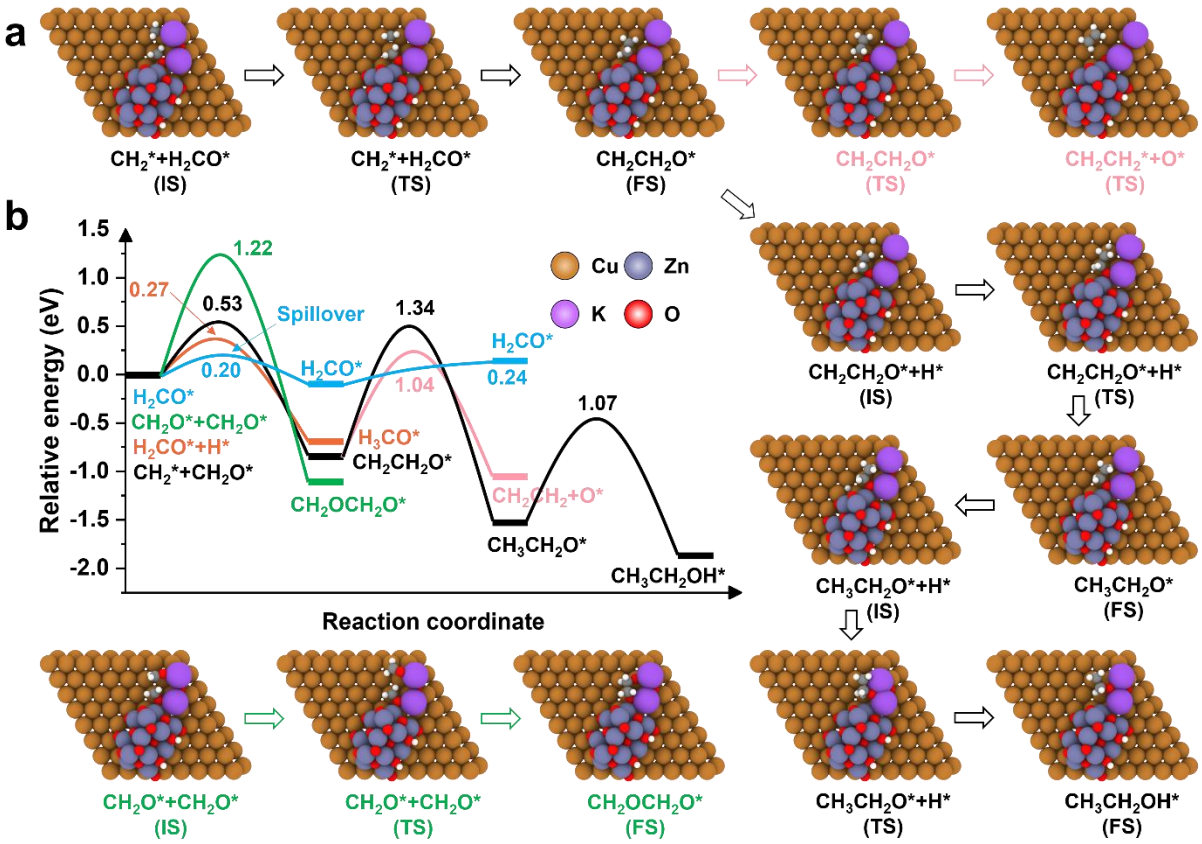

Supplementary Fig. 24. C-C coupling pathways on K_2O/Cu(111)/ZnO(101) surface. Reaction pathways of C-C coupling and the corresponding kinetic barrier of each elementary step on the interface of K_2O/Cu(111)/ZnO(101). For comparison, the energy barrier of spillover for CH_2O* species is also shown.

Note: Our experimental results indicated that the introduction of CZA can greatly promote the multi-carbon production on the Fe and FeCo catalysts. To further confirm the role of CZA as the reaction intermediates supplier instead of the key active center for the multi-carbon generation, we investigated the possible formation of dicarbon species on the CZA surface. Our computations indicated that, once the key intermediate of CH_2O* was formed, the couplings between CH_2* and CH_2O*, and two CH_2O* were energy unfavorable than the formation of CH_3O* species (0.27 eV) due to the large energy barrier of 0.53 and 1.22 eV, respectively. Thus, under the absence of Fe or FeCo catalysts, or the CH_2* species, CZA itself should mainly produce the single carbon product of CH_3COH. Once the CZA was interconnected with the Fe catalysts or the FeCo carbide, the low diffusion barrier of observed in the Supplementary Fig. 24 (ca. 0.20 to 0.24 eV) allowed the CH_2O* to go through a spillover process to supply plenty of CH_2O* to Fe catalysts or the FeCo carbide which accelerates the coupling process of CH_x* and CH_xO* on the carbides to enhance the $C_{2+}OH$ formation.

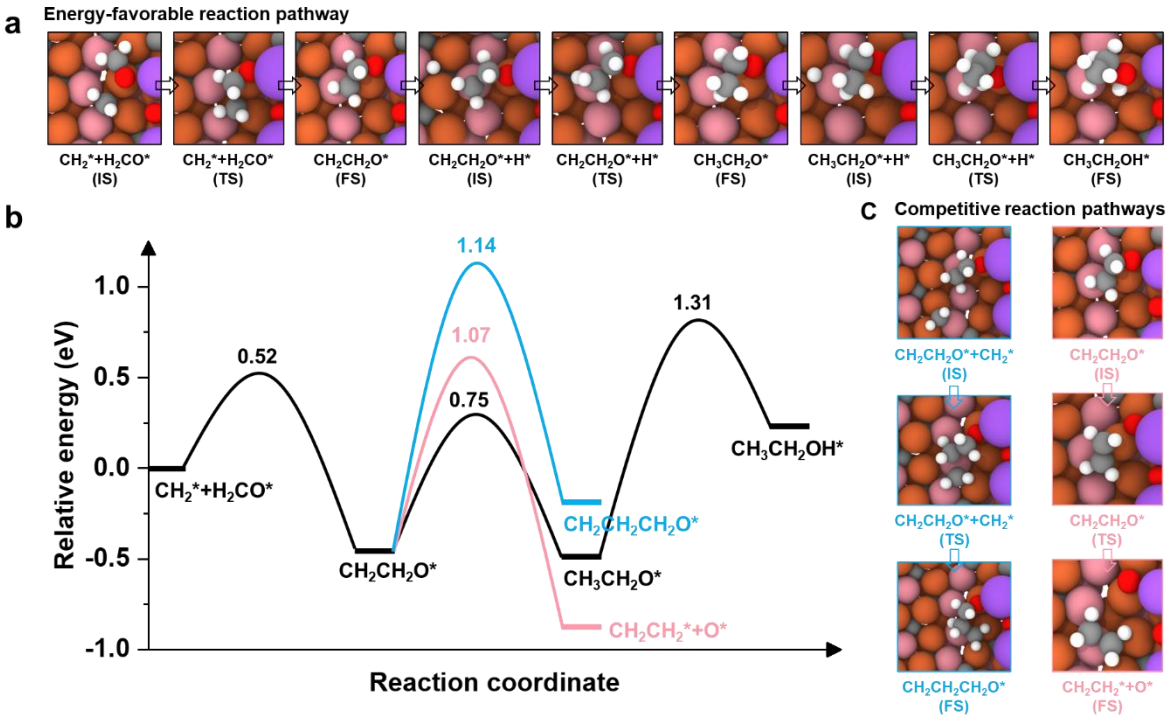

Supplementary Fig. 25. Energy barrier of carbon chain growth for $C_{2+}OH$ on $(Fe_{3/4}Co_{1/4})_5C_2(510)$ surface.

Note: To understand the underlying reason of improved C_2H_5OH selectivity on the FeCo carbide surface, we computed the competitive processes of generating other products during formation of C_2H_5OH. In detail, once the $CH_2CH_2O^*$ was formed, three possible pathways were considered, including: 1) $CH_2CH_2O^* + H^* \rightarrow CH_3CH_2O^*$, 2) $CH_2CH_2O^* \rightarrow CH_2CH_2O^* + O^*$, and 3) $CH_2CH_2O^* + CH_2^* \rightarrow CH_2CH_2CH_2O^*$, where the first pathway is the key step to generate C_2H_5OH, the second pathway is an unwanted step for producing hydrocarbons (e.g., C_2H_4), and the final pathway is the key step for the synthesis of $C_{3+}OH$ products. From Supplementary Fig. 25b, we can find that the energy barrier of these three steps were 0.75, 1.07, and 1.14 eV, respectively. Clearly, $CH_2CH_2O^*$ was more easily interact with H* to form the $CH_3CH_2O^*$ species, while the formation of the key intermediate of $CH_2CH_2CH_2O^*$ for the $C_{3+}OH$ production was prohibited due to a larger energy barrier of 1.14 eV. This reaction pathway preference renders the FeCo carbide a superior selectivity for the C_2H_5OH instead of other mixed alcohols.

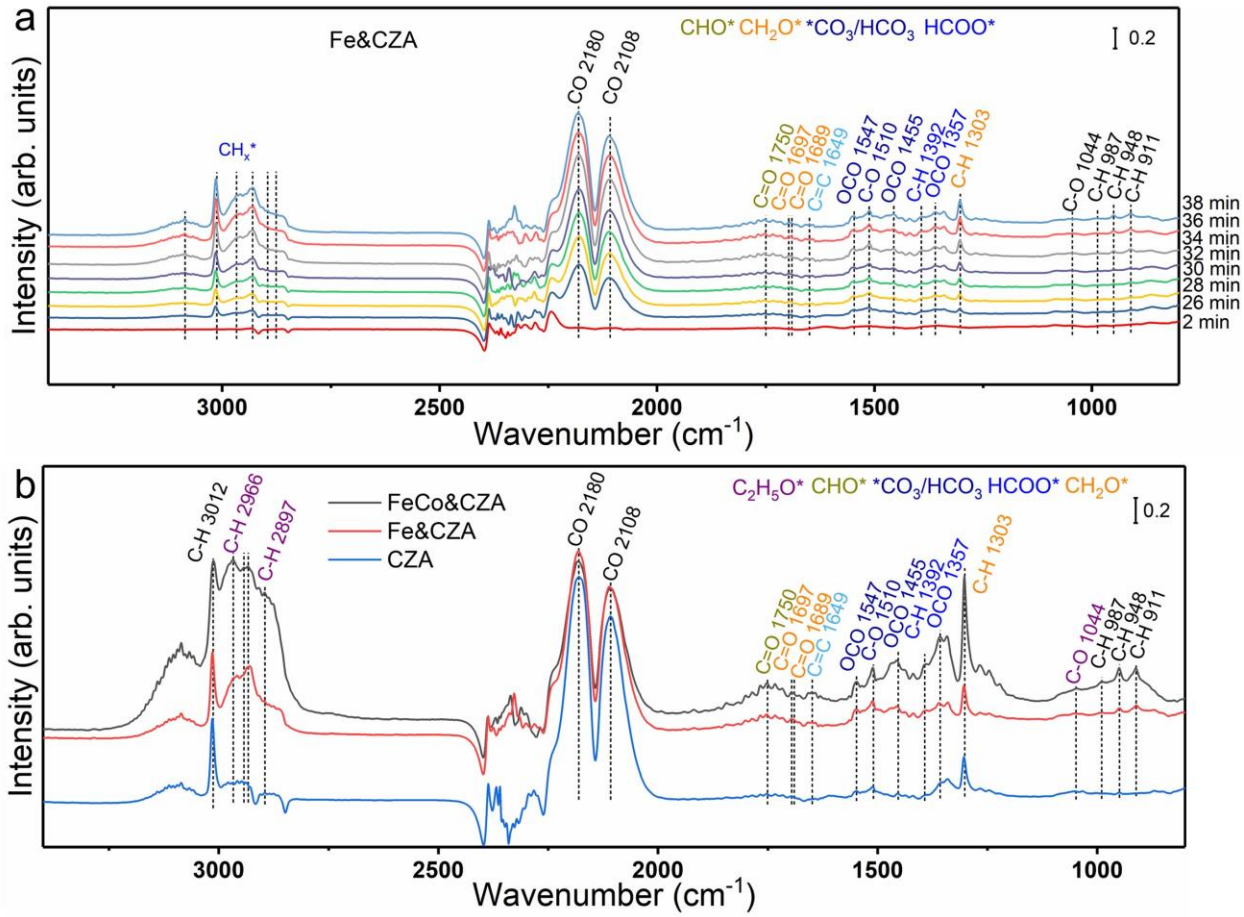

Supplementary Fig. 26. In-situ DRIFTS analysis of series catalysts. (a) In-situ DRIFTS of the Fe&CZA. (b) In-situ DRIFTS of FeCo&CZA, Fe&CZA and CZA at 38 min.

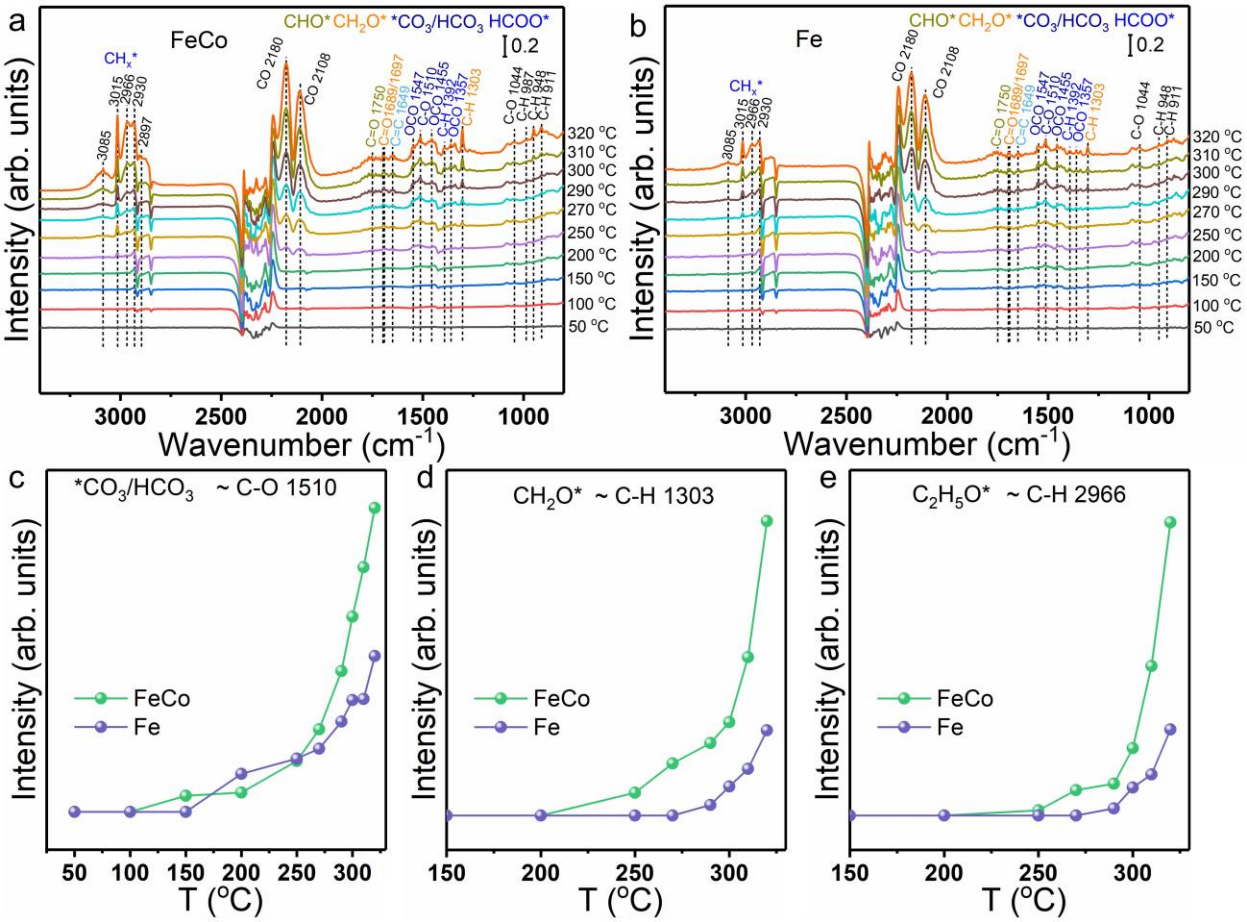

Supplementary Fig. 27. In-situ DRIFTS analysis of series catalysts. In-situ DRIFTS of (a) FeCo and (b) Fe catalysts at different temperature. (c-e) The peaks intensity on in-situ DRIFTS in FeCo and Fe catalysts at various temperature.

Supplementary Table 1. The performance of catalysts for CO_2 hydrogenation.

No.	Catalyst	X_{CO2}	S_{CO}	S_{HC}	Hydrocarbons				MeOH	$C_{2+}OH$	(Ethanol)	Others	$C_{2+}OH$ /ROH(%)	Yield of $C_{2+}OH$ (%)	$C_{2+}OH$ STY mg g_{cat}^{-1} h^{-1}
					$C_{2-4}^{=}$	$C_{5+}^{=}$	CH_4	Paraffin							
1	Fe/CZA	42.6	7.5	79.6	10.6	39.0	7.7	22.3	2.3	17.5	12.3	0.6	88.6	6.9	70.0
2	FeMn/CZA	40.9	8.6	73.6	12.0	39.3	7.5	14.7	3.5	22.5	17.4	0.4	86.6	8.4	86.4
3	FeZn/CZA	44.2	6.5	82.3	9.6	39.5	9.0	24.2	1.7	14.9	11.2	1.2	89.6	6.1	62.9
4	FeCo/CZA	42.3	6.4	70.1	14.5	30.0	12.2	13.4	3.1	26.2	19.0	0.6	89.4	10.4	105.6
5	FeCu/CZA	35.6	11.1	80.4	10.2	38.7	8.3	23.2	2.9	16.2	11.0	0.5	84.7	5.1	51.8

Reaction conditions:
320 ℃, 5.0 MPa, 0.2 g, H_2/CO_2 = 3:1, TOS = 8 h, gas hourly space velocity (GHSV) = 4500 ml^{-1} g_{cat}^{-1} h^{-1}.
Other: mainly aldehydes or esters.

$$C_{2+}OH/ROH = \frac{selectivity\ of\ C_{2+}OH}{selectivity\ of\ all\ alcohols}$$

Supplementary Table 2. The performance of catalysts for CO_2 hydrogenation.

No.	Catalyst	X_{CO2}	S_{CO}	S_{HC}	Hydrocarbons				MeOH	$C_{2+}OH$	(Ethanol)	Others	$C_{2+}OH$ /ROH(%)	Yield of $C_{2+}OH$ (%)	$C_{2+}OH$ STY mg g_{cat}^{-1} h^{-1}
					$C_{2-4}^{=}$	$C_{5+}^{=}$	CH_4	Paraffin							
1	FeCo&CZA	51.1	4.3	46.3	13.8	7.9	10.7	13.9	2.4	49.1	38.2	2.2	95.6	24.0	245.7
2	Fe&CZA	44.9	7.7	76.5	9.3	29.3	9.1	28.8	1.6	21.2	14.9	0.7	93.2	8.8	89.2
3	FeCo	37.4	6.0	85.9	25.8	22.5	17.9	19.7	1.7	12.0	9.0	0.4	88.1	4.2	86.1
4	Fe	36.2	5.9	84.7	19.3	31.9	12.5	21.0	2.0	12.5	9.4	0.8	86.8	4.3	87.6
5	FeCo||CZA	37.1	14.3	69.8	27.4	6.1	21.4	14.9	2.0	27.2	19.9	1.0	93.3	8.6	88.3
6	CZA||FeCo	43.7	6.9	77.9	17.2	20.4	11.6	28.7	6.5	14.4	10.7	1.2	70.8	5.9	59.9
7	FeCo(1:1)&CZA	49.0	5.5	69.4	6.9	16.8	17.2	28.5	1.3	28.4	21.2	0.9	95.7	13.1	134.3
8	FeCo(5:1)&CZA	46.9	7.2	58.3	5.6	23.4	7.2	22.2	2.6	37.6	26.9	1.5	93.7	16.4	166.1

Reaction conditions:
1-2, 5-8: 320 ℃, 5.0 MPa, 0.2 g, H_2/CO_2 = 3:1, TOS = 8 h, GHSV = 4500 ml^{-1} g_{cat}^{-1} h^{-1}.
3 and 4: 320 ℃, 5.0 MPa, 0.1 g, H_2/CO_2 = 3:1, TOS = 8 h, GHSV = 9000 ml^{-1} g_{cat}^{-1} h^{-1}.
Other: mainly aldehydes or esters.

$$C_{2+}OH/ROH = \frac{selectivity\ of\ C_{2+}OH}{selectivity\ of\ all\ alcohols}$$

Supplementary Table 3. Comparison of $C_{2+}OH$ synthesis performance of FeCo&CZA catalyst from CO_2 hydrogenation with other literature reported Fe-based catalysts.

No.	Catalysts	T (℃)	P (MPa)	GHSV (mL g_{cat}^{-1} h^{-1})	CO_2 Conv. (%)	CO Sel. (%)	$C_{2+}OH$ Sel. (%)	$C_{2+}OH$ STY (mg g_{cat}^{-1} h^{-1})	Ref.
1	Rh-Fe/SiO_2	260	5.0	6000	26.7	19.7	16.0*	65.8*	1
2	Rh-Fe/TiO_2	270	2.0	8000	9.2	28.4	6.4*	24.2*	2
3	RhFeLi/TiO_2	250	3.0	6000	15.7	12.5	31.3*	60.5*	3
4	K-CuMgZnFe	320	5.0	6000	30.3	30.6	22.9	69.6	4
5	CZK(1.5)//CFCK(4.5)	350	6.0	5000	32.4	45.3	11.8	72.4	5
6	Cs/Cu-Fe-Zn	330	5.0	4500	36.6	20	19.8	73.4	6
7	FeNaS-0.6	320	3.0	8000	32.0	20.7	12.8	78.5	7
8	K-CuMgZnFe/CZA	320	5.0	6000	42.3	13.8	20.2	106.5	8
9	K/Cu-Zn-Fe	300	7.0	5000	44.2	5.9	19.5*	110.6*	9
10	2%Na-Fe@C/5%K-CuZnAl	320	5.0	4500	39.2	9.4	40.9	132.1*	10
11	$ZnFe_2O_4$/Fe–Zn–Na[#]	320	5.0	12000	29.1	21.8	18.6	137.7	11
12	Cr(1%)-CuFe	320	4.0	6000	38.4	14.8	29.2	104.1	12
13	PdFe-6.9 (37 nm)	300	6.0	6000	33.3	27.9	19.1	86.5	13
14	FeCo&CZA	320	5	4500	**51.1**	4.3	**49.1**	**245.7**	This work

*：only ethanol

Supplementary Table 4. The performance of catalysts for CO_2 hydrogenation or syngas conversion.

No.	Catalyst	X_{CO2}	S_{CO}	S_{HC}	Hydrocarbons				MeOH	$C_{2+}OH$	(Ethanol)	Others	$C_{2+}OH$ /ROH(%)	Yield of $C_{2+}OH$ (%)	$C_{2+}OH$ STY mg g_{cat}^{-1} h^{-1}
					$C_{2-4}^{=}$	$C_{5+}^{=}$	CH_4	Paraffin							
1	FeCo&CZA-2:1	49.6	1.9	57.3	8.8	21.3	11.6	15.6	1.5	39.7	32.8	1.5	96.4	18.3	252.4
2	FeCo&CZA-4:1	39.2	3.1	64.4	12.4	20.2	14.2	17.6	1.2	33.4	27.2	1.0	96.4	12.7	209.5
3	FeCo&CZA-8:1	32.4	8.7	71.9	18.4	17.7	19.7	16.1	1.2	25.9	21.8	1.0	95.8	7.7	141.7
4	FeCo&CZA-16:1	26.1	15.4	74.2	21.3	15.1	21.9	15.9	1.4	21.7	17.2	2.7	93.9	4.8	93.0
5	Fe&CZA-2:1	38.0	4.6	74.3	11.5	30.6	10.9	21.3	1.2	23.5	18.4	1.0	95.3	8.5	116.7
6	Fe&CZA-4:1	37.4	3.9	77.6	13.0	30.5	11.6	22.5	1.0	20.1	14.9	1.3	95.3	7.2	118.0
7	Fe&CZA-8:1	35.2	7.3	76.0	15.3	28.7	12.8	19.2	1.1	20.3	15.8	2.6	94.7	6.6	120.9
8	Fe&CZA-16:1	32.1	6.2	77.8	16.2	29.2	15.2	17.2	1.0	18.7	14.2	2.5	94.7	5.6	108.6
9	Co	47.6	0.3	97.9	2.7	11.7	57.1	26.4	0.2	1.9	1.3	0	88.7	0.9	18.0
10	CZA	26.6	81.8	0.8	0.1	0	0.6	0.1	99.2	0	0	0	0	0	0
11	Co&CZA	45.3	1.5	89.3	6.4	8.2	56.4	17.3	1.6	9.2	7.0	0.9	85.5	4.1	83.9
12	FeCo&CZA	73.2 (X_{CO})	16.3 (S_{CO2})	74.4	4.3	27.5	11.5	28.6	1.0	24.6	18.9	1.1	96.0	15.1	213.2
13	FeCo&CZA	55.5	1.9	52.5	19.6	6.2	14.8	12.0	1.6	42.4	32.8	3.5	96.4	23.1	236.8

Reaction conditions:
1-4: 320 ℃, 5.0 MPa, FeCo catalyst of 0.1 g and the weight of CZA is 1/*x* of FeCo catalyst, H_2/CO_2 = 3:1, TOS = 8 h.
5-8: 320 ℃, 5.0 MPa, Fe catalyst of 0.1 g and the weight of CZA is 1/*x* of Fe catalyst, H_2/CO_2 = 3:1, TOS = 8 h.
9 and 10: 320 ℃, 5.0 MPa, 0.1 g, H_2/CO_2 = 3:1, TOS = 8h, GHSV = 9000 ml^{-1} g_{cat}^{-1} h^{-1}.
11 and 12: 320 ℃, 5.0 MPa, 0.2 g, H_2/CO_2 = 3:1 (*11*) and H_2/CO = 2:1 (*12*), TOS = 8h, GHSV = 4500 ml^{-1} g_{cat}^{-1} h^{-1}.
13: FeCo&CZA-catalyzed CO_2 hydrogenation reaction at a hundred-gram level fix-bed reactor. Reaction conditions: 320 ℃, 5.0 MPa, H_2/CO_2 = 3:1, TOS = 8 h, GHSV = 4500 ml^{-1} g_{cat}^{-1} h^{-1}.
Other: mainly aldehydes or esters. $C_{2+}OH/ROH = \frac{selectivity\ of\ C_{2+}OH}{selectivity\ of\ all\ alcohols}$

Supplementary Table 5. The performance of catalysts for CO_2 hydrogenation under different reaction condition.

No.	Temperature (°C)	Pressure (MPa)	X_{CO2}	S_{CO}	S_{HC}	Hydrocarbons				MeOH	$C_{2+}OH$	(Ethanol)	Others	$C_{2+}OH$ /ROH(%)	Yield of $C_{2+}OH$ (%)	$C_{2+}OH$ STY mg g_{cat}^{-1} h^{-1}
						$C_{2-4}^{=}$	$C_{5+}^{=}$	CH_4	Paraffin							
1	300	5	41.7	3.4	67.9	13.3	17.3	19.7	17.6	1.2	30.2	23.5	0.7	96.2	12.6	118.3
2	310	5	49.6	2.4	62.6	11.0	17.9	16.7	17.0	0.8	34.8	25.9	1.8	97.8	17.3	163.0
3	340	5	58.4	1.6	71.8	9.1	28.1	15.5	19.1	1.1	24.4	17.3	2.7	95.7	14.2	140.6
4	320	4	50.3	1.8	67.1	11.7	22.7	16.9	15.8	1.3	30.0	21.9	1.6	95.8	15.1	143.4
5	320	3	40.3	4.0	69.4	21.2	12.0	20.8	15.4	1.2	28.5	20.9	0.9	96.0	10.9	106.7

Reaction conditions: FeCo&CZA, 0.2 g, H_2/CO_2 = 3:1, TOS = 8 h, GHSV = 4500 ml^{-1} g_{cat}^{-1} h^{-1}.
Other: mainly aldehydes or esters.

$$C_{2+}OH/ROH = \frac{selectivity\ of\ C_{2+}OH}{selectivity\ of\ all\ alcohols}$$

Supplementary Table 6. Detailed ^{57}Fe Mössbauer parameters of various catalysts.

Catalyst	Phases	Mössbauer parameters			
		IS (mm/s)	QS (mm/s)	Hhf (kOe)	Area (%)
FeCo&CZA-spent	χ-Fe_5C_2	0.25	0.07	216	26.7
		0.23	0.02	185	26.7
		0.17	0.04	104	18.7
	Fe^{3+} (spm)	0.30	0.51	N.A.	17.3
	θ-Fe_3C	0.25	0.09	201	10.7
FeCo-spent	χ-Fe_5C_2	0.24	0.07	217	32.5
		0.20	0.05	184	32.5
		0.17	0.13	107	15.7
	Fe^{3+} (spm)	0.52	1.65	N.A.	8.1
	θ-Fe_3C	0.24	0.03	202	11.1
Fe&CZA-spent	χ-Fe_5C_2	0.25	0.11	218	22.6
		0.16	0.10	185	22.6
		0.20	0.13	109	5.6
	Fe^{3+} (spm)	0.29	0.97	N.A.	5.6
	Fe_3O_4	0.26	-0.02	488	7.1
		0.67	-0.04	452	28.5
Fe-spent	χ-Fe_5C_2	0.25	0.10	218	24.4
		0.17	0.07	181	24.4
		0.24	0.11	110	16.7
	θ-Fe_3C	0.18	0.07	197	8.4
	Fe^{3+} (spm)	0.36	1.08	N.A.	1.0
	Fe_3O_4	0.26	-0.01	490	8.2
		0.66	-0.02	458	16.9

Supplementary Table 7. The specific surface area and pore volume of catalysts.

No.	Sample	S_{BET} ($m^2 \cdot g^{-1}$)	S_{BET}^{Micro} ($m^2 \cdot g^{-1}$)	S_{BET}^{Meso} ($m^2 \cdot g^{-1}$)	V ($cm^3 \cdot g^{-1}$)
1	FeCo	83.1	6.2	76.9	0.178
2	FeCo-spent	5.0	0.7	4.3	0.019
3	Fe	49.0	10.2	38.8	0.361
4	Fe-spent	5.7	0.6	5.1	0.035

Supplementary Table 8. Structural parameters of the spent catalysts at the Fe K-edge extracted from the EXAFS fitting.

Sample	Path	CN	R(Å)	σ^2($\times10^{-3}$Å^2)	ΔE_0(eV)	R factor
Fe foil	Fe-Fe1	8	2.46	4.8	-3.8	0.010
	Fe-Fe2	6	2.84	5.1		
FeCo&CZA-spent	Fe-C	**1.5**	**1.98**	3.5	-5.0	0.009
	Fe-Co (Fe)	4.6	**2.57**	12.9		
FeCo-spent	Fe-C	**0.5**	**1.96**	0.3	0.2	0.002
	Fe-Co (Fe)	3.6	**2.56**	13.9		
Fe&CZA-spent	Fe-C (O)	**2.8**	**2.08**	11.6	2.6	0.019
	Fe-Fe1	3.8	**2.64**	17		
	Fe-Fe2	2.7	2.96	16		
	Fe-C (O)	2.7	3.51	1		
Fe-spent	Fe-C(O)	**1.6**	**2.07**	11.9	5.6	0.019
	Fe-Fe	1.9	**2.62**	12.7		
	Fe-C (O)	2	3.41	10.5		

(a) C*N*: coordination numbers; *R*: bond distance; σ^2: Debye-Waller factors; ΔE_0: the inner potential correction; *R* factor: goodness of fit; S_0^2, 0.8, was obtained from the experimental EXAFS fit of Fe foil reference by fixing CN as the known crystallographic value and was fixed to all the samples.

Supplementary Table 9. Structural parameters of the spent catalysts at the Co K-edge extracted from the EXAFS fitting.

Sample	Path	CN	R(Å)	σ^2($\times10^{-3}$Å^2)	ΔE_0(eV)	R factor
Co foil	Co-Co	12	2.49	6	0.8	0.004
FeCo&CZA-spent	Co-C	2	1.97	6.5	-2.54	0.003
	Co-Co (Fe)	12.1	2.58	16.0		
FeCo-spent	Co-C	0.9	1.92	0.3	-2.1	0.005
	Co-Co (Fe)	10.9	2.60	16.7		

(a) C*N*: coordination numbers; *R*: bond distance; σ^2: Debye-Waller factors; ΔE_0: the inner potential correction; *R* factor: goodness of fit; S_0^2, 0.8, was obtained from the experimental EXAFS fit of Co foil reference by fixing CN as the known crystallographic value and was fixed to all the samples.

Supplementary Table 10. Detailed ^{57}Fe Mössbauer parameters of catalysts after stability test.

Catalyst	Phases	Mössbauer parameters			
		IS (mm/s)	QS (mm/s)	Hhf (kOe)	Area (%)
FeCo&CZA-spent	χ-Fe_5C_2	0.22	0.07	213	32.5
		0.23	0.00	102	18.1
		0.19	0.05	186	20.1
	Fe^{3+} (spm)	0.34	0.49	N.A.	29.3
Fe&CZA-spent	χ-Fe_5C_2	0.28	0.00	236	15.4
		0.33	0.00	176	14.0
		0.10	0.00	96	20.1
	Fe^{3+} (spm)	0.26	0.42	N.A.	19.0
	θ-Fe_3C	0.23	0.07	204	25.2
	Fe_3O_4	0.20	-0.10	480	2.0
		0.65	-0.10	445	4.3
FeCo&CZA-spent-1000h	χ-Fe_5C_2	0.15	0.00	99	23.9
		0.23	0.00	181	25.6
		0.23	0.00	208	25.6
	Fe^{3+} (spm)	0.24	0.63	N.A.	24.9

Supplementary Table 11. Reaction mechanism of CO_2 hydrogenation on the Site 1 of $(Fe_{3/4}Co_{1/4})_5C_2(510)$ surface. The kinetic favorable pathways are highlighted by blue color.

Reaction pathway	Reaction barrier (eV)	Reaction heat (eV)
CO_2 (g) + * → CO_2*	N/A	-0.73
CO_2* + H* → HCOO*	0.91	0.15
CO_2* + H* → COOH*	1.49	0.91
CO_2* → CO* + O*	1.07	0.12
CO* + H* → COH*	1.83	1.12
CO* + H* → CHO*	1.20	0.96
HCOO* + H* → CH_2OO*	2.17	1.58
HCOO* + H* → HCOOH*	1.39	0.97
HCOO* → CHO* + O*	2.99	1.16
HCOOH* → CHO* + OH*	0.73	-0.35
CHO* +OH* + H* → CHO* + H_2O*	0.97	0.07
CHO* + H_2O* → CHO* + H_2O (l)	N/A	0.88
CHO* + H* → CH_2O*	0.52	0.30
CHO* + H* → CHOH*	2.37	0.16
CH_2O* + H* → CH_3O*	0.77	0.41
CH_2O* → CH_2* + O*	1.32	-0.28
CH_3O* + H* → CH_3OH*	1.07	0.60
CH_2* + O* + H* → CH_2* + OH*	0.74	-0.46
CH_2* + OH* + H* → CH_2* + H_2O*	0.73	-0.13
CH_2* + H_2O* → CH_2* + H_2O (l)	N/A	0.92
CH_2* + H* → CH_3*	0.44	-0.18
CH_3* + H* → CH_4*	0.98	0.29

Supplementary Table 12. Reaction mechanism of CO_2 hydrogenation on the Site 2 of $(Fe_{3/4}Co_{1/4})_5C_2(510)$ surface. The kinetic favorable pathways are highlighted by blue color.

Reaction pathway	Reaction barrier (eV)	Reaction heat (eV)
CO_2 (g) + * → CO_2*	N/A	-1.00
CO_2* + H* → HCOO*	0.63	0.43
CO_2* + H* → COOH*	1.40	0.71
CO_2* → CO* + O*	0.74	-0.14
CO* + H* → COH*	1.85	0.89
CO* + H* → CHO*	1.34	1.11
HCOO* → CHO* + O*	1.18	0.36
HCOO* + H* → HCOOH*	0.92	0.88
HCOO* + H* → CH_2OO*	1.14	0.75
HCOOH* → CHO* + OH*	0.62	-0.53
CHO* + OH* + H* → CHO* + H_2O*	1.22	0.60
CHO* + H_2O* → CHO* + H_2O (l)	N/A	1.11
CHO* + H* → CH_2O*	0.66	0.60
CHO* + H* → CHOH*	1.75	1.03
CH_2O* + H* → CH_3O*	0.65	-0.13
CH_2O* → CH_2* + O*	0.41	-0.24
CH_2* + O* + H* → CH_2* + OH*	1.26	-0.19
CH_2* + OH* + H* → CH_2* + H_2O*	1.31	0.58
CH_2* + H_2O* → CH_2* + H_2O (l)	N/A	0.86
CH_2* + H* → CH_3*	1.06	0.74
CH_3* + H* → CH_4*	1.25	0.21

Supplementary Table 13. Reaction mechanism of CO_2 hydrogenation on the Site 1 of $Fe_5C_2(510)$ surface. The kinetic favorable pathways are highlighted by blue color.

Reaction pathway	Reaction barrier (eV)	Reaction heat (eV)
CO_2 (g) + * → CO_2*	N/A	-0.75
CO_2* + H* → HCOO*	0.84	0.39
CO_2* + H* → COOH*	1.50	1.01
CO_2* → CO* + O*	1.43	0.05
CO* + H* → COH*	1.80	1.26
CO* + H* → CHO*	0.95	0.93
HCOO* → CHO* + O*	0.83	-0.17
HCOO* + H* → HCOOH*	1.27	0.84
CHO* + O* → CHO* + OH*	0.94	-0.80
CHO* +OH* + H* → CHO* + H_2O*	0.91	-0.11
CHO* + H_2O* → CHO* +H_2O (l)	N/A	0.96
CHO* + H* → CH_2CO*	0.56	0.29
CH_2O* + H* → CH_3O*	0.97	0.39
CH_2O* → CH_2* + O*	0.96	0.33
CH_2* + O* + H* → CH_2* + OH*	1.23	-0.61
CH_2* + OH* + H* → CH_2* + H_2O*	0.66	-0.25
CH_2* + H_2O* → CH_2* + H_2O (l)	N/A	1.17
CH_2* + H* → CH_3*	0.18	-0.36
CH_3* + H* → CH_4*	0.95	0.08

Supplementary Table 14. Reaction mechanism of CO_2 hydrogenation on the Site 2 of $Fe_5C_2(510)$ surface. The kinetic favorable pathways are highlighted by blue color.

Reaction pathway	Reaction barrier (eV)	Reaction heat (eV)
CO_2 (g) + * → CO_2*	N/A	-1.91
CO_2* + H* → HCOO*	0.87	0.61
CO_2* + H* → COOH*	1.57	0.78
CO_2* → CO* + O*	0.64	-0.45
CO* + O* + H* → CO* + OH*	1.48	0.62
CO* + OH* + H* → CO* + H_2O*	1.01	-0.05
CO* + H_2O* → CO* + H_2O (l)	N/A	1.25
CO* + H* → CHO*	0.97	0.80
CHO* → CH* + O*	0.32	-0.59
CHO* + H* → CH_2O*	0.66	0.52
CH* + O* + H* → CH* + OH*	1.10	-0.37
CH* + OH* + H* → CH* + H_2O*	1.15	0.47
CH* + H_2O* → CH* + H_2O (l)	N/A	0.88
CH* + H* → CH_2*	0.93	0.88
CH_2* + H* → CH_3*	0.73	0.65
CH_3* + H* → CH_4*	1.15	0.19

Note: Similar to the $(Fe_{3/4}Co_{1/4})_5C_2(510)$, we identified two active sites for the CO_2* adsorption, including Site 1 where the adsorbates interact with $Fe_5C_2(510)$ via three Fe atoms, and Site 2 in which the reaction species can form four bonds with neighboring four Fe atoms. To unveil the inferior selectivity for $C_{2+}OH$ production on $Fe_5C_2(510)$ surface and to identify the key reaction species for the C-C coupling, the reaction pathways of CO_2 hydrogenation toward single carbon products were systematically investigated (Figs. 3c and 3d, the detailed energy barrier can be found in Supplementary Tables 13 and 14).

On the Site 1, CO_2 molecule was found to be adsorbed through an energy downhill process by releasing energy of 0.75 eV. After adsorption, CO_2* preferred to couple with one of H* to form HCOO* after overcoming an energy barrier of 0.84 eV. In comparison, the direct dissociation into CO* and O* (CO_2* → CO* + O*) and protonation into COOH* (CO_2* + H* → COOH*) were energetically unfavorable in terms of the larger energy battier of 1.43 and 1.50 eV, respectively. After HCOO* was formed, the dissociation of HCOO* into CHO* + O* readily occurred due to the strong oxophilicity of Fe sites with an energy input of 0.83 eV, while the hydrogenation of HCOO* into HCOOH* (HCOO* + H* → HCOOH*) was mostly prohibited by a larger barrier of 1.27 eV. Once the CHO* and O* were generated, O* could be reduced into H_2O* by coupling with two H* with the energy requirement of 0.94 eV for the O* hydrogenation, and 0.91 eV for the OH* reduction. Then, the generated H_2O* desorbed from the surface after overcoming a barrier of 0.96 eV. After the desorption of H_2O*, the hydrogenation of CHO* into CH_2O* occurred with a relatively small barrier of 0.56 eV. Subsequently, the CH_2O* can be converted to CH_3O* (CH_2O* + H* → CH_3O*) or dissociated into CH_2* and O* (CH_2O* → CH_2* + O*). The dissociation barrier was computed to be 0.96 eV, 0.01 eV lower than the generation of CH_3O* species. Thus, CH_2* and O* were expected to dominate at the surface followed by the CH_3O*, and the further reduction

of O* and CH_2* into H_2O and CH_4* were preferred via four hydrogenation steps. The largest barrier of 1.23 eV was found at O* reduction, and therefore the OH* formation step (CH_2* + O* + H* → CH_2* + OH*) was identified as the rate-limiting step. We noted that the catalytic selectivity of CO_2 hydrogenation on the Site 1 was very different from the $(Fe_{3/4}Co_{1/4})_5C_2(510)$, in which CH_2O* was found to overcome a barrier of 0.77 eV to form the CH_3O* and the dissociation into CH_2* and O* was effectively suppressed by a lager barrier of 1.32 eV. Thus, it is expected that the insufficient stabilization of CH_2O* than the CH_2* might be a reason of the inferior $C_{2+}OH$ synthesis performance of $Fe_5C_2(510)$.

On Site 2 of $Fe_5C_2(510)$, CO_2 adsorption became more energetically favorable than on Site 1 due to more unsaturated Fe sites, as indicated by the more negative adsorption energy of -1.91 eV. After the adsorption, CO_2* preferred to dissociate to CO* and O* by overcoming an energy barrier of 0.64 eV, whereas the formation of HCOO* and COOH* were suppressed with the higher energy barrier of 0.87 and 1.57 eV, respectively. Next, the dissociated O* species could be reduced into H_2O* via two continuous steps (CO* + O* + H* → CO* + OH* and CO* + OH* + H* → CO* + H_2O*) with the energy barrier of 1.48 and 1.01 eV, respectively. Then the formed H_2O* overcame 1.25 eV for the desorption, leaving the CO* on Site 2. In the following step, the CO* could be hydrogenated into CHO* after overcoming an energy barrier of 0.97 eV. Particularly, due to the strong oxophilicity of Fe sites, CHO* dissociated into CH* and O* species with a very small barrier of 0.32 eV. On the contrary, the formation of CH_2O* was prohibited in terms of a larger energy requirement of 0.66 eV. Subsequently, the H_2O* formed by the reduction of O*, and the energy barriers for the hydrogenation of O* and OH* were found to be 1.10 and 1.15 eV, respectively. After the H_2O* desorption, CH* could be hydrogenated into CH_4* by coupling three H* species, and the energy input for the CH* + H* → CH_2*, CH_2* + H* → CH_3*, and CH_3* + H* → CH_4* were 0.93, 0.73, and 1.15 eV, respectively. As a result, the rate-limiting step was identified as the CO* + O* → CO* + OH* due to the largest barrier of 1.48 eV.

In general, our computations indicated that both of Site 1 and Sites 2 on the $Fe_5C_2(510)$ preferred to catalyze CO_2 into CH_x* due to the strong oxophilicity of Fe sites that offer strong capability of dissociating CH_xO*. The reduced generation of key CH_xO* relative to the $(Fe_{3/4}Co_{1/4})_5C_2(510)$ could be the major reason for the inferior $C_{2+}OH$ production. Moreover, we then investigated the possible coupling between CH_2* with the other species, including CO*, CHO*, and CH_2O* (Fig. 3f, the detailed energy barrier can be found in Supplementary Table 17). We found that even though the CH_2* easily coupled with CH_2O* species to form the CH_2CH_2O* with a small energy barrier of 0.30 eV, the hydrogenation of CH_2CH_2O* (CH_2CH_2O* + H* → CH_3CH_2O*) was more energetically unfavorable than the dissociation (CH_2CH_2O* → C_2H_4* + O*) step. Specifically, the dissociation barrier was computed to be 0.51 eV, lower than that of 0.62 eV for the further hydrogenation (CH_2CH_2O* + H* → CH_3CH_2O*). Thus, such pathway preference and insufficient stabilization for the CH_2O* and CH_2CH_2O* species strongly reduced its ability for $C_{2+}OH$ production, and resulted in the lower $C_{2+}OH$ yield by comparison with the $(Fe_{3/4}Co_{1/4})_5C_2(510)$.

Supplementary Table 15. Reaction mechanism of CO_2 hydrogenation on the interface of K_2O/Cu(111)/ZnO(101). The kinetic favorable pathways are highlighted by blue color.

Reaction pathway	Reaction barrier (eV)	Reaction heat (eV)
CO_2 (g) + * → CO_2*	N/A	-0.80
CO_2* + H* → HCOO*	0.63	-0.79
CO_2* + H* → COOH*	1.06	-0.11
CO_2* → CO* + O*	1.14	0.18
HCOO* + H* → CH_2OO*	0.87	0.63
HCOO* + H* → HCOOH*	1.10	0.60
HCOO* → CHO* + O*	2.32	2.14
CH_2OO* → CH_2O* + O*	0.86	0.68
CH_2O* + O* + H* → CH_2O* + OH*	1.03	-0.68
CH_2O* + OH* + H* → CH_2O* + H_2O*	0.79	0.38
CH_2O* + H_2O* → CH_2O* + H_2O (l)	N/A	0.89
CH_2O* + H* → CH_3O*	0.27	-0.69
CH_3O* + H* → CH_3OH*	0.88	-0.32

Note: To unveil the role of CZA in $C_{2+}OH$ synthesis from CO_2 hydrogenation, the reaction mechanism of CO_2 reduction into single carbon products on the interface of K_2O/Cu(111)/ZnO(101) was studied (Fig. 4a, Supplementary Table 15). Our computations indicated that the adsorption of CO_2 on the interface was energetically favorable with a downhill energy of -0.80 eV. Once the CO_2* was formed, CO_2* was readily protonated by H* to form HCOO* with an energy barrier of 0.63 eV. The direct dissociation (CO_2* → CO* + O*) and the protonation to COOH* (CO_2* + H* → COOH*) were mostly prohibited due to the larger energy barrier of 1.14 and 1.06 eV, respectively. In the subsequent step, HCOO* preferred to couple with H* to form CH_2OO* after overcoming an energy barrier of 0.87 eV, while larger energy inputs of 1.10 and 2.32 eV were necessary for the formation of HCOOH* and CHO*+O*, respectively. Next, the reaction could go through a dissociation step (CH_2OO* → CH_2O* + O*) with an energy barrier of 0.86 eV. After the formation of O* adsorbates, O* could be reduced into water molecules by coupling two H* species with the energy requirements of 1.03 and 0.79 eV, respectively, leaving the CH_2O* on the CZA surface. Then, the desorption of H_2O occurred after overcoming the desorption barrier of 0.89 eV. In the following steps, CH_2O* was easily to be hydrogenated to CH_3O* with a small energy barrier of 0.27 eV, and the CH_3OH was found to be the final product after overcoming a barrier of 0.88 eV. Overall, the CZA preferred to catalyze the CO_2 hydrogenation via the following steps: CO_2* → HCOO* → CH_2OO* → CH_2O* + O* → CH_2O* + OH* → CH_2O* + H_2O* → CH_2O* +H_2O (l) → CH_3O* → CH_3OH* → CH_3OH (l). The rate limiting step was identified as the CH_2O* + O* → CH_2O* + OH* with the largest energy barrier of 1.03 eV.

Supplementary Table 16. Reaction mechanism of C-C coupling on the $(Fe_{3/4}Co_{1/4})_5C_2(510)$ surface. The kinetic favorable pathways are highlighted by blue color.

Reaction pathway	Reaction barrier (eV)	Reaction heat (eV)
CH_2* + CO* → CH_2CHO*	0.87	0.66
CH_2* + CHO* → CH_2CHO*	1.17	-1.03
CH_2* + CH_2O* → CH_2CHO*	0.52	-0.48
CH_3* + CO* → CH_2CHO*	1.03	0.30
CO* + CO* → COCO*	N/A	N/A
CH_2CO* + H* → CH_2CHO*	0.64	0.23
CH_2CHO* + H* → CH_2CH_2O*	1.24	0.93
CH_2CH_2O* + H* → CH_3CH_2O*	0.75	0.12
CH_2CH_2O* + H* → CH_2CH_2OH*	1.32	0.64
CH_2CH_2O* → C_2H_4* + O*	1.07	-0.39
CH_3CH_2O* + H* → CH_3CH_2OH*	1.31	0.72

Supplementary Table 17. Reaction mechanism of C-C coupling on the Fe_5C_2(510) surface. The kinetic favorable pathways are highlighted by blue color.

Reaction pathway	Reaction barrier (eV)	Reaction heat (eV)
CH_2* + CO* → CH_2CHO*	0.76	0.47
CH_2* + CHO* → CH_2CHO*	1.41	-0.70
CH_2* + CH_2O* → CH_2CHO*	0.30	-0.47
CO* + CO* → COCO*	N/A	N/A
CH_2CO* + H* → CH_2CHO*	0.70	-0.09
CH_2CHO* + H* → CH_2CH_2O*	1.03	0.98
CH_2CHO* + H* → CH_2CHOH*	1.40	1.05
CH_2CH_2O* + H* → CH_3CH_2O*	0.62	-0.05
CH_2CH_2O* → C_2H_4* + O*	0.51	-0.40
CH_3CH_2O* + H* → CH_3CH_2OH*	1.41	0.73

Supplementary Table 18. Stream results of the whole process.

Stream	S7	S8	S9	S10	S11	S12	S13	S14	S15	S16	S17	S18	S19	S20	S21	S22	S23	S24	S25	S29	S44	S45
H_2(Mole Frac)	0	1	0.75	0.75	0.75	0.43	0.43	0.43	0.43	0.77	0	0	0	0	0	0	0	0	0	0	0	0
C1~C4(Mole Frac)	0	0	0	0	0	0.05	0.05	0.05	0.05	0.065	0.04	0.04	0.21	0	0.029	0.23	0	0	0	0	0	0
H_2O(Mole Frac)	0	0	0	0	0	0.33	0.33	0.33	0.33	0.003	0.74	0.74	0.05	0	0.85	0.836	0.92	0	0.21	0	0.08	0
CO_2(Mole Frac)	1	0	0.25	0.25	0.25	0.15	0.15	0.15	0.15	0.16	0.14	0.14	0.68	0.02	0.05	0.77	0	0	0	0	0	0
CH_4O(Mole Frac)	0	0	0	0	0	0	0	0	0	0	0	0	0	0.02	0.008	0	0.008	0.99	0.001	0	0	0
C_2H_6O(Mole Frac)	0	0	0	0	0	0.027	0.027	0.027	0.027	0.001	0.06	0.06	0.03	0.01	0.06	0.105	0.06	0	0.78	0.99	0.04	0
C_3H_8O(Mole Frac)	0	0	0	0	0	0.004	0.004	0.004	0.004	0	0.008	0.008	0	0	0.009	0	0.009	0	0.008	0	0.87	0
$C_4H_{10}O$(Mole Frac)	0	0	0	0	0	0.001	0.001	0.001	0.001	0	0.002	0.002	0	0	0.002	0	0.002	0	0	0	0	0.67
$C_5H_{12}O$(Mole Frac)	0	0	0	0	0	0.0005	0.0005	0.0005	0.0005	0	0.001	0.001	0	0	0.001	0	0.001	0	0	0	0	0.32
C_8H_{18}(Mole Frac)	0	0	0	0	0	0.003	0.003	0.003	0.003	0.001	0.005	0.005	0.03	0.93	0.95	0	0	0	0	0	0	0
Total Flow (kmol/h)	1000	3000	4000	4000	4000	2954.1	2954.1	2954.1	2954.1	1311	1643.1	1643.1	189.6	0.3	1204.1	81.8	1122.9	0.3	91	71	11.6	4.2
Temperature (℃)	85.5	85	78	241	320	320	150	137	40	40	40	22	35	35	35	16.1	87.2	63.7	78.0	77.9	92.5	122.8
Pressure (bar)	50	50	50	50	50	50	50	20	20	20	20	1	1	1	1	1	1	1	1	1	1	1

Supplementary Table 19. Economic analysis of a plant with an annual capacity of 200,000 tons of CO_2.

No.	Project	Cost (million $)	Note
a	Raw material	47.30	Refer to Table 18
b	Fuel and power	9.32	Refer to Table 19
c	Manufacturing cost	3.36	Refer to Table 20
d	Wage and welfare expenses	0.22	
A	Production cost	60.20	a + b + c + d
e	Management cost	0.07	
f	Financial expenses	0.47	
g	Cost of sales	0.87	Annual sales income *1~3%
B	Full cost	61.61	A + e + f + g
C	Average annual sales revenue	76.76	Refer to Table 21
D	Average annual sales tax	9.83	Refer to Table 22
E	Total annual profit	5.32	C – B – D
F	Average annual income tax	1.33	E*0.25
G	After-tax profits	3.99	E – F

Supplementary Table 20. Consumption of raw materials and catalysts.

Project	Total Consumption (t)	Unit price ($/t)	Cost (million $)
H_2	30,000	1383.13	41.49
CO_2	200,000	27.66	5.53
Catalyst	10	27662.52	0.28

Supplementary Table 21. Consumption of public works.

Project	Annual consumption	Unit price ($)	Cost (million $)
Electricity	5600 kW·h	0.09	5.03
Saturated steam	19.2 t	16.60	3.19
Recycled water	3600 t	0.03	1.10

Supplementary Table 22. Detailed explanation of manufacturing cost.

Project	Depreciation Cost (million $)	Repair cost (million $)	Other manufacturing Cost (million $)
Manufacturing cost	2.32	0.90	0.14

Supplementary Table 23. Sales of products.

No.	Product	Unit price ($/t)	Sales volume (t)	Total amount (Million $)
1	$Alkane_{C1\sim C4}$, C_{5+}	968.19	26300	25.46
2	$C_2^{=}\sim C_4^{=}$	1106.50	11000	12.17
3	C_2H_6O	878.28	30000	26.35
4	C_3H_8O	1175.66	5600	6.58
5	Other alcohols	1106.50	5600	6.20
		Total		76.76

Supplementary Table 24. The estimates of commodity turnover tax through Chinese policies.

No.	Project	Cost (Million $)
1	Value-added tax (VAT) = Output VAT - Input VAT	8.94
1.1	Output VAT	10.97
1.1.1	Ethylene, propylene and gasoline (17%)	10.25
1.1.2	C_4 products (13%)	0.71
1.2	Input VAT	2.03
1.2.1	Steam, circulating water, fuel gas, etc. (13%)	0.49
1.2.2	Other raw and auxiliary materials and electricity (17%)	1.54
2	Tax for maintaining and building cities (7%)	0.63
3	Education supplementary tax (3%)	0.27

Note: Technical and economic analyses (TEA) were performed with the ethanol production plant with an annual capacity of 200,000 tons of CO_2 as an example (process details illustrated in Fig. 6d, and Supplementary Tables 18-24), in which the annual output of ethanol and olefins is about 30,000 and 10,000 tons, respectively. The process flow diagram is depicted in Fig. 6d. The mass balance and stream results of the process are listed in Supplementary Table 18. It is estimated that the total investment of the whole project is 33.47 million US$. On the basis of the simulation results, we calculated the cost, revenue, and profit (Supplementary Tables 19-24). According to Aspen plus simulation results by Wison Company, the total products cost are 61.61 million US$, and the annual sales income of products are 76.76 million US$ (see Supplementary Table 23 for details) by 8000 h $year^{-1}$ of operation. Therefore, the total after-tax profit (Based on Chinese policy) of all products is 3.99 million US$ per year.

Furthermore, we found that the feasibility of the ethanol plant depended heavily on the price of reactant gas (H_2 and CO_2). The cost of H_2 and CO_2 accounted for 67.3% and 9.0% of the total cost (Fig. 6e). The process would be economically viable with H_2 prices lower than 1.6 US$ kg^{-1} at a CO_2 price of 27.7 US$ ton^{-1} (Fig. 6f). Similarly, when the current H_2 price was fixed at 1.4 US$ kg^{-1}, CO_2 prices lower than 54.2 US$ kg^{-1} would obtain a positive revenue. Carbon tax, as a vital factor of effect CO_2 price, was further analyzed (Fig. 6g). Carbon tax of 40-80 $ ton^{-1} is required to meet the temperature goals of the Pairs Agreement[45], while the cost of CO_2 as raw material will become lower and lower with the advancement of government policies and the continuous development of carbon capture technology. The price range of below 1.6 US$ kg^{-1} is currently only feasible for blue/grey H_2 from fossil fuels[46]. According to the forecast of International Renewable Energy Agency (IRENA) and the Hydrogen Council[43, 44], the cost of H_2 production will become lower and lower with the advancement of government policies and the continuous development of hydrogen production technology. The cost of H_2 production from renewable energy (green hydrogen) will drop to 1 US$ kg^{-1} by 2050.

Supplementary Table 25. The element content in the catalysts by inductive coupled plasma-atomic emission spectroscopy (ICP-AES).

Element	Fe (wt%)	Co (wt%)	Na (wt%)
Fe	53.5	-	2.5
FeCo (5:1)	43.8	9.4	3.8
FeCo (3:1)	43.6	16.0	3.4
FeCo (1:1)	27.7	29.7	3.4

Supplementary References

1. Kusama, H.; Okabe, K.; Sayama, K. & Arakawa, H. Ethanol synthesis by catalytic hydrogenation of CO_2 over Rh-$FeSiO_2$ catalysts. *Energy* **22**, 343-348, (1997).
2. Gogate, M. R. & Davis, R. J. Comparative study of CO and CO_2 hydrogenation over supported Rh-Fe catalysts. *Catal. Commun.* **11**, 901-906, (2010).
3. Yang, C.; Mu, R.; Wang, G.; Song, J.; Tian, H.; Zhao, Z.-J. & Gong, J. Hydroxyl-mediated ethanol selectivity of CO_2 hydrogenation. *Chem. Sci.* **10**, 3161-3167, (2019).
4. Xu, D.; Ding, M.; Hong, X. & Liu, G. Mechanistic aspects of the role of K promotion on Cu-Fe-based catalysts for higher alcohol synthesis from CO_2 hydrogenation. *ACS Catal.* **10**, 14516-14526, (2020).
5. Guo, H.; Li, S.; Peng, F.; Zhang, H.; Xiong, L.; Huang, C.; Wang, C. & Chen, X. Roles investigation of promoters in K/Cu-Zn catalyst and higher alcohols synthesis from CO_2 hydrogenation over a novel two-stage bed catalyst combination system. *Catal. Lett.* **145**, 620-630, (2014).
6. Xu, D.; Ding, M.; Hong, X.; Liu, G. & Tsang, S. C. E. Selective C_{2+} alcohol synthesis from direct CO_2 hydrogenation over a Cs-promoted Cu-Fe-Zn catalyst. *ACS Catal.* **10**, 5250-5260, (2020).
7. Yao, R.; Wei, J.; Ge, Q.; Xu, J.; Han, Y.; Ma, Q.; Xu, H. & Sun, J. Monometallic iron catalysts with synergistic Na and S for higher alcohols synthesis via CO_2 hydrogenation. *Appl. Catal. B: Environ.* **298**, 120556, (2021).
8. Xu, D.; Yang, H.; Hong, X.; Liu, G. & Tsang, S. C. E. Tandem catalysis of direct CO_2 hydrogenation to higher alcohols. *ACS Catal.* **11**, 8978-8984, (2021).
9. Takagawa, M.; Okamoto, A.; Fujimura, H.; Izawa, Y. & Arakawa, H. Ethanol synthesis from carbon dioxide and hydrogen. *Stud. Surf. Sci. Catal.* **114**, 525-528, (1998).
10. Wang, Y.; Wang, K.; Zhang, B.; Peng, X.; Gao, X.; Yang, G.; Hu, H.; Wu, M. & Tsubaki, N. Direct conversion of CO_2 to ethanol boosted by intimacy-sensitive multifunctional catalysts. *ACS Catal.* **11**, 11742-11753, (2021).
11. Yang, H.; Wei, Z.; Zhang, J.; Dang, Y.; Li, S.; Bu, X.; Zhou, Z.; Gong, C.; Wang, H.; Li, J.; Liu, Y.; Yang, Y.; Xiao, T.; Liu, C.; Sun, Y. & Gao, P. Tuning the selectivity of CO_2 hydrogenation to alcohols by crystal structure engineering. *Chem* **10**, 2245-2265, (2024).
12. Zhang, Q.; Wang, S.; Geng, R.; Wang, P.; Dong, M.; Wang, J. & Fan, W. Hydrogenation of CO_2 to higher alcohols on an efficient Cr-modified CuFe catalyst. *Appl. Catal. B: Environ.* **337**, 123013, (2023).
13. Wang, Y.; Zhou, Y.; Zhang, X.; Wang, M.; Liu, T.; Wei, J.; Zhang, G.; Hong, X. & Liu, G. PdFe Alloy-Fe_5C_2 interfaces for efficient CO_2 hydrogenation to higher alcohols. *Appl. Catal. B: Environ.* **345**, 123691, (2024).